Experimental Investigation of the Effects of a Passing Shock on Compressor Stator Flow

Matthew D. Langford

Thesis submitted to the Faculty of the Virginia Polytechnic Institute and State University in partial fulfillment of the requirements for the degree of

Master of Science

in

Mechanical Engineering

Dr. Wing Ng, Chair

Dr. Clint Dancey

Dr. Joseph Schetz

April 17, 2003

Blacksburg, VA

Keywords: Compressor Cascade, Particle Image Velocimetry, Rotor Bow Shock, Unsteady Losses, Vortex Formation.

Experimental Investigation of the Effects of a Passing Shock on Compressor Stator Flow

Matthew D. Langford

(Abstract)

A stator cascade was developed to simulate the flow conditions within a close-stage-spacing transonic axial compressor. Experiments were conducted in a linear transonic blowdown cascade wind tunnel with an inlet Mach number of 0.65. The bow shock from the downstream rotor was simulated by a single moving normal shock generated with a shock tube. First, steady pressure data were gathered to ensure that the stator cascade operated properly without the presence of the shock. Next, the effects of the passing shock on the stator flow field were investigated using shadowgraph photography and Digital Particle Image Velocimetry (DPIV). Measurements were taken for three different shock strengths. In every case studied, a vortex formed near the stator trailing edge as the shock impacted the blade. The size of this vortex was shown to be directly related to the shock strength, and the vortex remained present in the trailing edge flow field throughout the cycle duration. Analysis of the DPIV data showed that the vortex acts as a flow blockage, with the extent of this blockage ranging from 2.9% of the passage for the weakest shock, to 14.3% of the passage for the strongest shock. The vortex was also shown to cause flow deviation up to 75° for the case with the strongest shock. Further analysis estimated that the total pressure losses due to shock-induced vorticity ranged from 46% to 113% of the steady wake losses. Finally, the total pressure loss purely due to the upstream-propagating normal shock was estimated to be roughly 0.22%.

Acknowledgements

I would like to thank Dr. Wing Ng for the opportunities he has given me throughout my career as a student at Virginia Tech. He has always pushed me to succeed while giving me the freedom to choose my own path. I would also like to thank Dr. Clint Dancey for introducing me to the exciting field of compressible flow and Dr. Joseph Schetz for his advice on flow visualization and unsteady loss estimation, and both for serving on my advisory committee.

Special thanks to Andy Breeze-Stringfellow, William Solomon, and everyone at GE Aircraft Engines Fan and Compressor Aero for providing the funding for this project and sharing their knowledge with me. Thanks to Yingzhi Zhang, Susan Brewton, David Botos, and Greg Whitaker. Stephen Guillot provided invaluable experimental and writing advice. Greg Dudding, Gary Dudding, and Monte Lentner never ceased to amaze me with their top-notch craftsmanship while on a tight schedule.

Fellow graduate students at Virginia Tech also provided immense help on this project. Thanks to Austin Smith, Drew Nix, Shiming Li, and Bo Song for sharing their extensive wind tunnel experience. I am also grateful to Severin Kempf for his Fieldview assistance.

Thanks to Steve Edwards of the AOE Electronics Shop for his support throughout the project. He single-handedly solved just about every instrumentation problem I came across. Thanks to Dr. Jordi Estevadeordal of ISSI for gathering and processing the DPIV data.

I am grateful to my parents, John and Joanne, my sister Bree, and all my friends for their continued support. Finally, I would like to thank my Catherine for tolerating the weeks at a time I vanished into the depths of the wind tunnel and for her writing guidance.

Table of Contents

Index of Figures

Index of Tables

Index of Equations

Nomenclature

Acronyms

A/D	Analog to Digital
AFRL	Air Force Research Laboratory
CAD	Computer-Aided Design
CFD	Computational Fluid Dynamics
DPIV	Digital Particle Image Velocimetry
TE	Trailing Edge
TTL	Transistor-Transistor Logic

Variables

a	Acoustic Velocity
$\frac{dS}{dn}$	Entropy Gradient Normal to the Streamline
$\frac{dh_0}{dn}$	Stagnation Enthalpy Gradient Normal to the Streamline
k	Gladstone-Dale Coefficient
M_1	Upstream Mach Number Relative to Moving Shock
M_2	Downstream Mach Number Relative to Moving Shock
M_i	Inlet Mach Number
$\overline{P_1}$	Average Inlet Static Pressure
P_{01}	Inlet Stagnation Pressure
P_{02}	Downstream Angle Probe Stagnation Pressure
Ps_1	Static Pressure Upstream of Shock
Ps_2	Static Pressure Downstream of Shock
Pst_1	Initial Shock Tube Driven Section Pressure
Pst_2	Shock Tube Pressure Behind Propagating Shock
Pst_3	Shock Tube Pressure Behind Expansion Wave
Pst_4	Initial Shock Tube Driver Section Pressure
n	Index of Refraction
R	Gas Constant
R_C	Streamline Radius of Curvature

T_1 Static Temperature Upstream of Shock

T_2 Static Temperature Downstream of Shock

u Velocity in x-direction

v Velocity in y-direction

V_1 Absolute Velocity Upstream of Shock

V_2 Absolute Velocity Downstream of Shock

V_S Absolute Shock Velocity

y Cascade Pitch

Greek

ζ Local Vorticity Magnitude

ζ_{AV} Average Vorticity Magnitude

γ Specific Heat Ratio

ρ Density

ψ Stream Function

ω Local Total Pressure Loss Coefficient

Chapter 1.0: Introduction

1.1: Background and Motivation

The desire within the aircraft engine industry to decrease engine weight and size while increasing thrust has led to ever-closer stage spacing within transonic compressors. A transonic compressor is defined to be an axial flow compressor in which the inlet Mach number relative to the rotor blades varies from subsonic values near the hub to supersonic values near the blade tips. For damage tolerance reasons, transonic rotor leading edges are required to be slightly blunt (rather than perfectly sharp). A consequence of this geometry is the generation of a detached bow shock which resides upstream of the rotor leading edge and follows the rotor blades as they rotate (Kerrebrock, 1981). This shock, an example of which may be seen in Figure 1.1, provides the majority of the static pressure rise across the transonic rotor row, and its oblique incidence relative to the inlet flow generally keeps losses low.

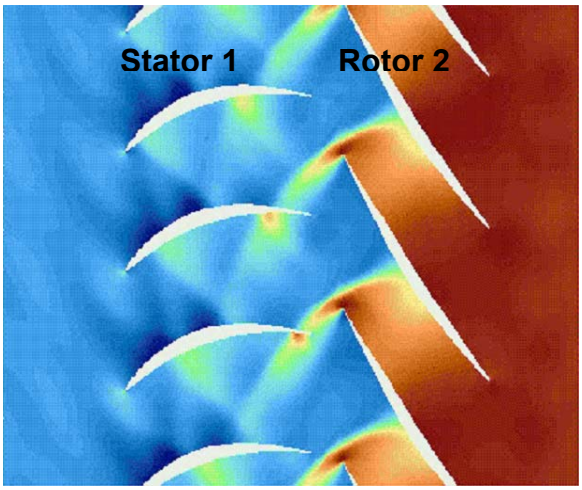

Image courtesy of GE Aircraft Engines

Figure 1.1: Static pressure contours from a 2-D CFD solution of a transonic compressor showing the rotor bow shock/stator interaction.

The losses incurred due to rotor shocks are generally acceptable when compared with the benefits of using transonic rotors. However, recent rig tests of close-stage-spacing transonic compressors have led to the discovery of unexpectedly high losses within the first-stage stator row. For the particular compressor of interest, the first two

stages operate with transonic rotors, while flow heating due to compression causes later stages to operate entirely subsonic. Because the first-stage stator row is the only stator row in the compressor with a transonic rotor row directly downstream from it, it was concluded that the stator losses must be due to an interaction with the bow shock from the downstream rotor. The rotating rig environment does not lend itself to affordable instrumentation and flow visualization, so studying the effects of a passing shock on compressor stator flow within the simpler linear cascade environment is the objective of the current work.

The issue of transonic rotor-stator interactions has been a topic of both experimental and analytical research recently. The general consensus among these researchers is that the losses in transonic compressors increase rapidly as axial spacing between stages is reduced. The following section summarizes the findings of a few selected publications on the topic of transonic rotor-stator interactions.

1.2: Previous Research

1.2.1: CFD Simulation of an Upstream Propagation Shock from a Transonic Rotor

Prasad (2003) developed a numerical simulation of the upstream-propagating shock waves from the isolated compressor designated NASA Rotor-35. Prasad compared viscous numerical results to a semi-analytical acoustic model and concluded that the shock wave evolution is primarily an inviscid phenomenon. The shock-induced circumferential pressure distortion near the stator trailing edge for an isolated rotor was compared to results for the same rotor imbedded in a time-accurate multi-stage simulation, leading Prasad to conclude, "…that one may use the induced pressure distortion generated by an isolated rotor to obtain conservative preliminary estimates for the distortion experienced by the upstream stator trailing edge flow in a multi-stage environment." In addition, it was shown that to maintain a given level of induced pressure distortion, the axial spacing required between a transonic/supersonic rotor and its upstream stator must be nearly twice that required for a subsonic compressor.

1.2.2: Experimental Study of the Effect of Blade-row Spacing on Performance

Gorrell et al. (2002) conducted an experimental investigation of the effect of blade-row spacing on the performance of a transonic compressor using the U.S. Air Force Research Laboratory's Stage Matching Investigation (SMI) rig. Mass flow rate, pressure ratio, and efficiency all decreased as the axial spacing between the upstream wake generator and the transonic rotor was decreased. At close spacing, an additional loss beyond mixing losses was present.

Part 2 of the paper presents CFD results for the same wake generator/transonic rotor system used in the experiment. At far axial spacing between the wake generator row and the rotor row, the rotor bow shock has degenerated into a pressure wave by the time it reaches the wake generator surface and is simply blocked. At close axial spacing, however, the bow shock turns normal to the wake generator surface as it passes the trailing edge and propagates upstream. The wake generator flow is supersonic relative to this moving wave and thus it acts like a normal shock, causing significant entropy generation and total pressure loss.

1.2.3: DPIV Study of Wake-Blade Interaction in a Transonic Compressor

Estevadeordal et al. (2002) documented the flow field within a transonic compressor using Digital Particle Image Velocimetry (DPIV). This experimental study also took place at the AFRL SMI rig. Data were gathered for two span-wise locations, two different wake generator counts, and two axial spacings between wake generator and rotor.

The wake generators (WGs) in this test had blunt trailing edges, which led to vortex shedding in the wake. These vortices were larger at 75% span than at 90% span, largely due to casing boundary layer interactions and higher turbulence levels at 90% span. The WG count determined the vortex path; for the 24 WG count, the vortex interacting with the rotor leading edge did not always impact directly. However, at the 40 WG count, this same vortex is always destroyed as the rotor "chops" it. Twice as many vortices pass between the rotor blades for the 24 WG count as compared to the 40 WG count. The vortices were also found to grow as they convected downstream. For the greater axial spacing, the vortices are estimated to be 30% larger than the WG thickness.

While the vortex generation itself is a function of the WG geometry, the vortex shedding frequency was largely dictated by the rotor blade passing frequency. Flow patterns such as the number and location of the vortices were always similar for a given rotor blade passing frequency. The rotor bow shocks provide a strong periodic pressure fluctuation that forces the synchronization of the vortex shedding to the shock-passing frequency.

1.3: Outline

Simulating the complex flow environment of a transonic compressor within a linear cascade of a single stator row is a difficult challenge. Before any unsteady results may be considered, the stator cascade must be shown to be operating correctly under steady loading (no shock). Data gathered from a downstream angle probe traverse will be presented to quantify the steady performance of the stator row. The total pressure losses for a range of incidence angles will also be shown. Finally, blade surface static pressure distributions will be presented for a range of incidence angles.

The first task for the unsteady portion of the experiment is to demonstrate that the moving shock in the experiment matches the orientation of the rotor bow shock in the actual compressor. Both shadowgraph images and wall static pressure measurements will be used for this purpose. The static pressure rise across the moving shock in the cascade will also be compared to the shock in the actual compressor.

Once the steady operation of the cascade has been validated and the shock has been proven to compare favorably to the desired conditions, the effects of the passing shock on the stator flow field will be discussed. A sequence of shadowgraph images from the shock-passing event will be presented and compared with DPIV velocity vector fields. Analysis of the DPIV data will be performed in order to identify the primary unsteady loss mechanisms and estimate the extent of the unsteady losses.

The following section details the facility, equipment, and instrumentation used in the experiment. Next, the steady performance of the stator cascade will be investigated. Unsteady measurements of the shock and its effects on the stator flow field will then be presented. Finally, the unsteady results will be analyzed to estimate the shock-induced losses within the stator row.

Chapter 2.0: Experimental Setup

2.1: Wind Tunnel Facility

The tests took place at the Virginia Tech Transonic Cascade Wind Tunnel. It is a blow-down type tunnel, providing up to 20 seconds of usable run time for the inlet Mach number used in this experiment. A four-stage Ingersoll-Rand type H reciprocating compressor provides the air supply for the tunnel. Before entering the tunnel, the air is filtered, cooled, dried, and stored in outdoor tanks. The tunnel is run by a computer-controlled main valve and simple feedback electronics. Figure 2.1 is a CAD drawing of the cascade test section in the wind tunnel.

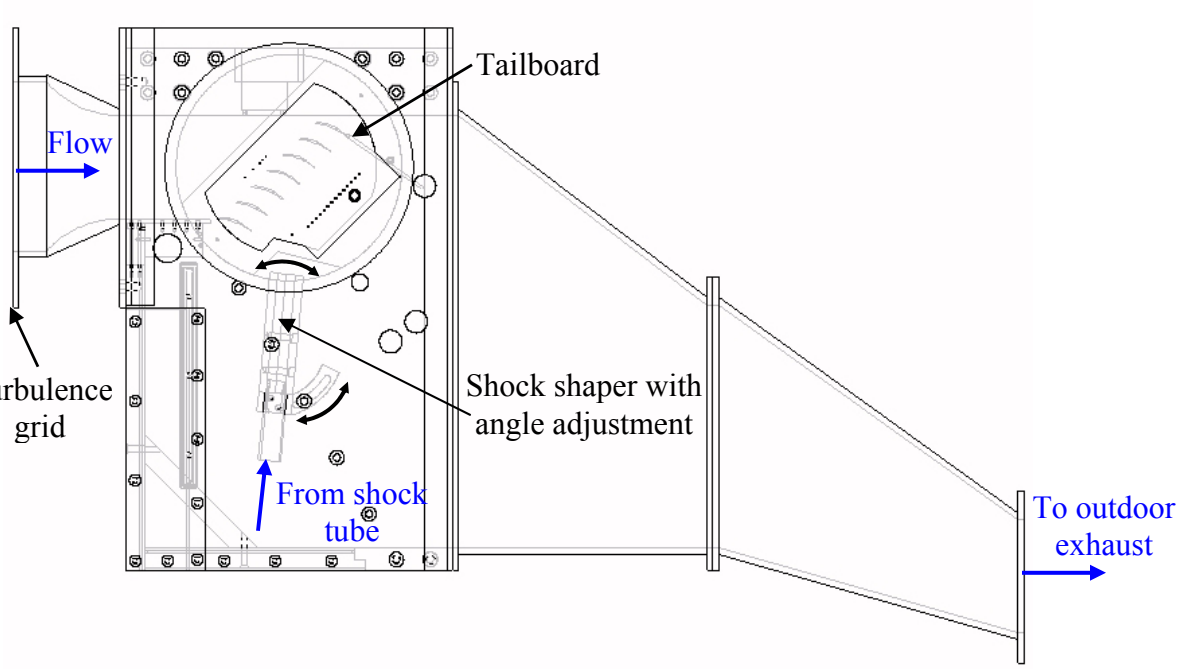

Figure 2.1: CAD drawing of the cascade test section in the Virginia Tech Transonic Cascade Wind Tunnel.

Tailboards are typically used in this facility to improve flow periodicity in the pitch-wise direction. However, this cascade has only an upper tailboard tangent to the trailing edge of the top blade (there is no tailboard downstream of the lowest blade). A lower tailboard would have obstructed the introduction of the shock.

A turbulence grid is mounted directly upstream of the test section. This grid consists of overlapping 7/16 in. diameter steel rods. Douglas (2001) provides a detailed description of the grid design process and subsequent flow measurements. Douglas concluded the turbulence intensity at the blade row inlet for this grid at M=0.65 is approximately 1.6%, with a length scale of 1.7 cm.

The shock is introduced to the test section through a shock shaper apparatus, which will be discussed in detail in a later section. The shock shaper is mounted to the test section walls and may be rotated to achieve various shock orientations before being bolted in place. The shock shaper connects to the external shock tube via a ten foot long section of reinforced tubing that passes through a hole in the bottom of the test section.

2.2: Cascade Stator Blades

Although the blade profile of the stators in the actual compressor varies extensively in the radial direction, a typical blade profile near mid-span was chosen for the cascade tests. The blade chord was scaled up by a factor of 2.75 to match the scale of the wind tunnel test section. Table 2.1 describes the key parameters for the cascade.

Table 2.1: Cascade parameters.

Blade chord (in.)	2.998
Blade span (in.)	6.0
Blade pitch (in.)	1.983
Solidity	1.512
Blade turning angle	35°
Cascade angle	45°
Inlet Mach number	0.65
Number of blades	7

The cascade stator has a 0.030 in. endwall clearance from 50% chord to the trailing edge. This clearance allows a small amount of leakage flow from the pressure surface to the suction surface, helping to prevent corner separation. The blades are mounted to the acrylic test section windows using four 0.125 in. diameter pins. A CAD rendering of the cascade stator geometry may be seen in Figure 2.2.

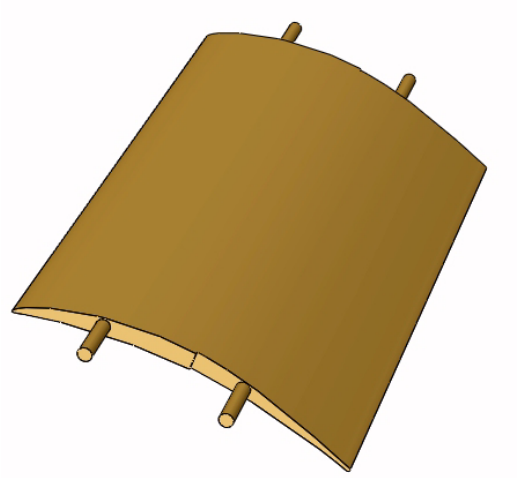

Figure 2.2: Cascade stator geometry.

2.3: Shock Tube

The moving shock is generated by rupturing a Mylar diaphragm within a pressurized shock tube and transferring the resulting shock into the test section. The shock tube consists of two sections of three-inch nominal diameter steel pipe separated by the diaphragm. The driver section is five feet long and the driven section is ten feet long. Figure 2.3 shows a diagram of the shock tube assembly.

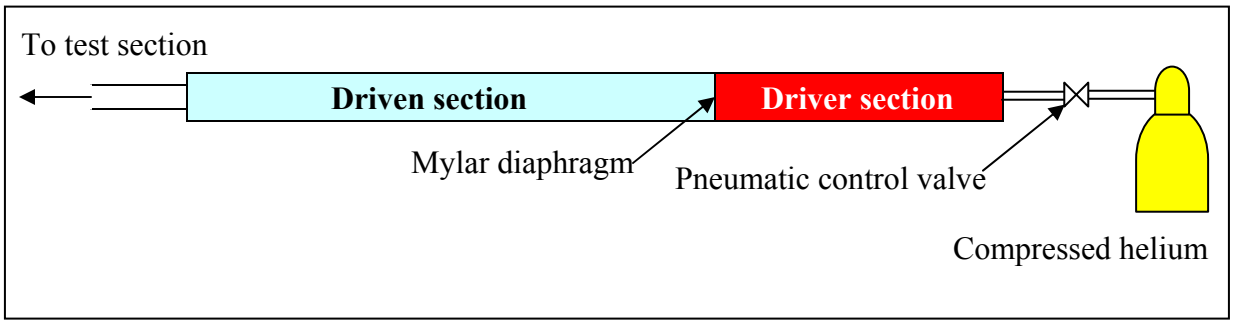

Figure 2.3: Shock tube schematic.

To initiate the shock, the driver section is rapidly compressed with helium until the diaphragm ruptures. The static pressure ratio across the propagating shock within the shock tube (Pst_2/Pst_1) is given by the following implicit function (Anderson, 1982):

Equation 2.1

$$\frac{Pst_4}{Pst_1} = \frac{Pst_2}{Pst_1}\left\{1 - \frac{(\gamma_4 - 1)(a_1/a_4)(Pst_2/Pst_1 - 1)}{\sqrt{2\gamma_1\left[2\gamma_1 + (\gamma_1 + 1)(Pst_2/Pst_1 - 1)\right]}}\right\}^{-2\gamma_4/(\gamma_4 - 1)}$$

Evaluation of Equation 2.1 shows that, for a given diaphragm pressure ratio (Pst_4/Pst_1), the propagating shock strength (Pst_2/Pst_1) will increase as the acoustic velocity ratio across the diaphragm (a_1/a_4) decreases. The driven section is open to the wind tunnel, so it contains air with a_1 approximately equal to 343 m/s. Helium is used for the driver gas because it provides a high a_4 (approximately 1000 m/s), resulting in a higher propagating shock strength for a lower driver section pressure.

Mylar diaphragm material was available in two thicknesses: 0.003 in. and 0.007 in. Doughty (1994) found the rupture pressure of a Mylar diaphragm within this shock tube to be approximately 20 psi per thousandth of an inch thickness. By stacking multiple diaphragms, a variety of rupture pressures could be achieved.

2.4: Shock Shaper

After the shock is fully developed within the driver section of the shock tube, it is transmitted through the flexible reinforced tubing into the test section. Before being introduced into the cascade, the shock is passes through the shock shaper, which is shown in Figure 2.4. The purpose of the shock shaper is to expand the circular shock in such a way that the wave becomes purely cylindrical (i.e. 2-dimensional), rather than spherical, as it passes the stator blades.

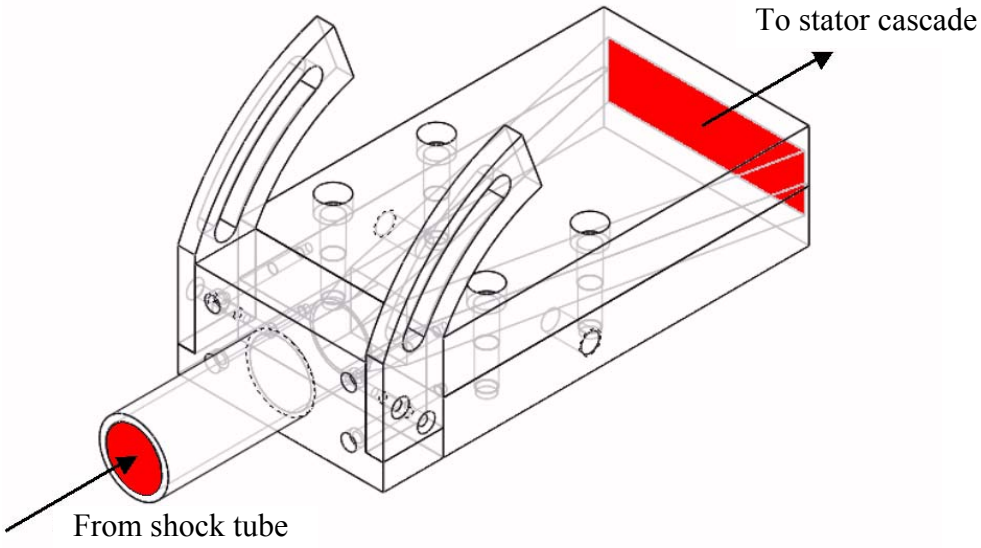

Figure 2.4: Shock shaper assembly.

The design of the shock shaper was based on a similar apparatus developed by Doughty (1994) for the purpose of turbine shock research. After consulting publications by Chester (1960), Nettleton (1973), and Sloan (1975), Doughty chose to use a tapered shock shaper with a divergence angle of 24 degrees. This angle minimized side-wall reflections and other disturbances behind the shock. It was also necessary that the exit plane of the shock shaper be nearly the same width as the test section span, to minimize wall reflections as the shock propagated through the test section. The shock shaper designed for the current experiment used the same 24-degree divergence angle as Doughty's design, while improving the internal wall smoothness and adding the capability to easily adjust the shock angle.

2.5: Instrumentation and Data Acquisition

2.5.1: Steady Pressure Measurements

The steady pressure measurements for this experiment may be divided into three categories: upstream of the blade row, downstream of the blade row, and blade surface. Figure 2.5 is a labeled rendering of the steady measurement locations in the test section.

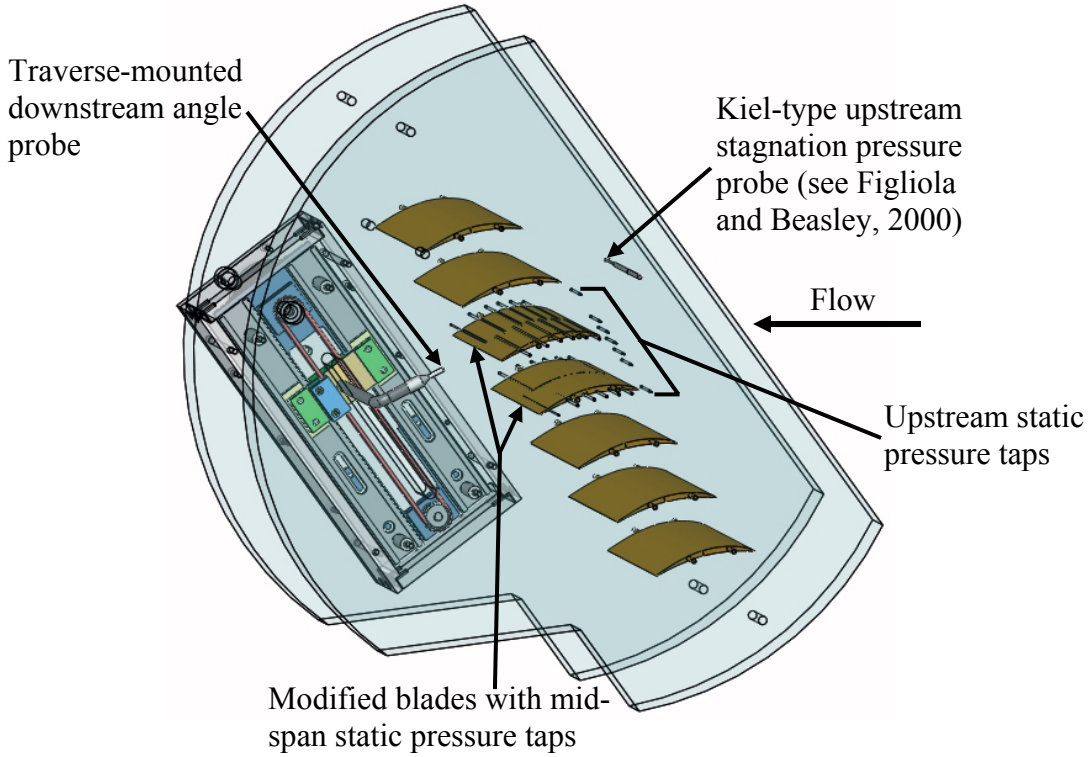

Figure 2.5: Labeled rendering of steady measurement locations in the test section.

The primary purpose of the upstream measurements is to establish the inlet Mach number for a given run. For all runs, the intended inlet Mach number was 0.65. The average wall static pressure from the seven upstream static pressure taps, $\overline{P}_1$, and the mid-span inlet stagnation pressure from the Kiel-type probe, P_{01}, are related to the inlet Mach number by the following relationship:

Equation 2.2

$$M_i = \sqrt{\left(\frac{2}{\gamma - 1}\right)\left[\left(\frac{P_{01}}{\overline{P}_1}\right)^{\frac{\gamma-1}{\gamma}} - 1\right]}$$

(Oosthuizen and Carscallen, 1997)

The center blade in the cascade is machined to have twelve static pressure taps distributed along the suction surface at mid-span. The next blade up has twelve taps distributed along the pressure surface at mid-span. These static pressure taps allow the blade surface static pressure distribution to be measured for a single passage in the cascade. Figure 2.6 is a photograph of the blades instrumented to measure blade surface static pressure mounted in the test section.

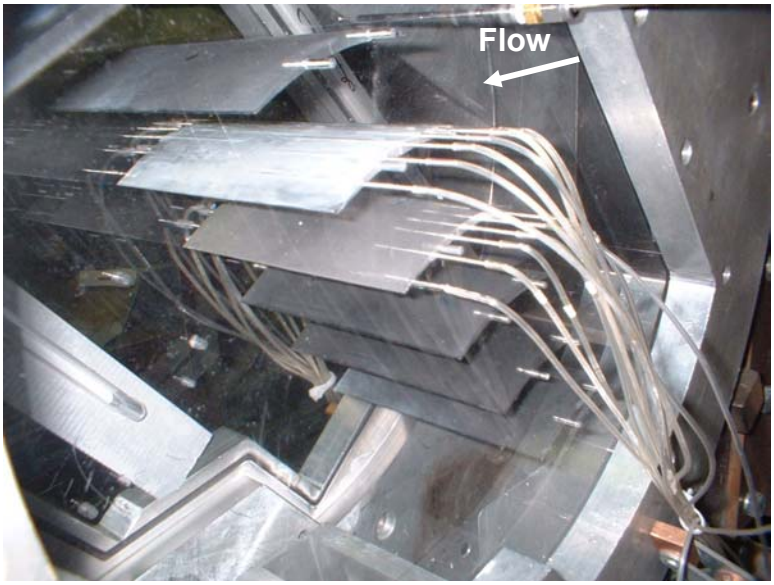

Figure 2.6: Blades instrumented to measure the blade surface static pressure distribution.

Steady downstream data are gathered using a traverse-mounted 3-port angle probe. The head of this probe is located approximately 45% chord downstream from the

stator trailing edge. The center port on the angle probe measures the local stagnation pressure, but the upper and lower ports are placed on inclined surfaces and thus measure components of both stagnation and static pressure. These pressure measurements may then be reduced to determine the flow angle distribution along the traverse axis. Stagnation pressure losses in the stator wakes may also be quantified by directly measuring the pressure differential between the Kiel probe at the inlet and the stagnation pressure port on the angle probe. For all downstream measurements, the traverse moved at a linear speed of 0.5 in./sec over a distance of about 4 inches.

2.5.2: Unsteady Pressure Measurements

In addition to measuring the pressure at various points in the flow under steady loading, the wall static pressure at specific points was measured for runs involving the moving shock. The primary purpose of these measurements was to provide boundary conditions to use in future unsteady CFD simulations of the shock/cascade system. However, this information would also be used to measure the shock strength and orientation.

The transducer locations for the unsteady wall static pressure measurements may be seen in Figure 2.7. Due to the limited availability of high-frequency transducers and signal amplifiers, measurements were only taken at four of these locations in a given run.

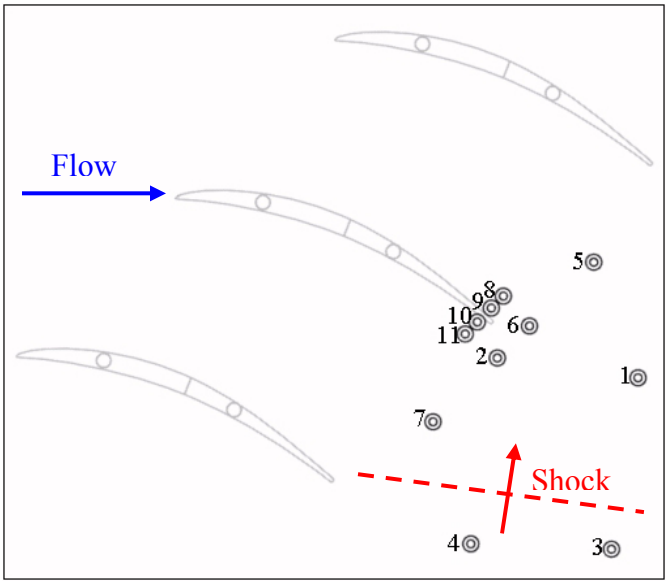

Figure 2.7: Transducer locations for unsteady shock pressure measurements.

2.5.3: Transducers and Data Acquisition Systems

The measurements for this experiment required a broad range of transducers and data acquisition systems. Quantities such as the inlet stagnation pressure, inlet static pressure, and blade surface static pressure remained relatively steady throughout the run, and thus did not require high frequency response transducers or high A/D sample rates. The downstream angle probe measured relatively steady pressures, but the probe was traversed through a spatially-varying pressure field, so the transducer frequency response and A/D sample rate became more important. Finally, for measurements involving the moving shock, extremely high transducer frequency response and A/D sample rates were required to accurately capture the rapidly-varying pressure field due to the shock.

A Pressure Systems International (PSI) 8400 system was used for upstream pressure and blade surface pressure measurements. It provides the best uncertainty of the available transducer options, at the expense of relatively poor frequency response. The system has a built-in 16-bit A/D converter. Downstream measurements required improved transducer rise times to capture the large stagnation pressure gradients in the wakes, so MKS transducers were used. These transducers were connected to a 16-bit National Instruments A/D converter and sampled at 500 Hz. Kulite transducers with an ultra-high natural frequency of 500 kHz were used for the unsteady shock pressure measurements. The Kulite data was sampled at 1 MHz using a 12-bit LeCroy 6810 A/D converter. Table 2.2 is a summary of the transducers and A/D systems used for the various pressure measurements.

Table 2.2: A/D systems and transducers used for various pressure measurements.

	Upstream/Blade Surface Measurements	**Downstream Measurements**	**Wall Shock Measurements**
A/D	Pressure Systems International 8400	National Instruments AT-MIO-16XE-50	LeCroy 6810
Transducers	0-15 psid	MKS 0-3 psid and 0-20 psid	Kulite XCL-072 0-50 psig
Sample Rate	50 Hz	500 Hz	1 MHz
Uncertainty	± .001 psi	± .005 psi (0-3) ± .01 psi (0-20)	± .05 psi

2.6: Shadowgraphy System

Shadowgraph images respond to the second spatial derivative, or Laplacian, of the fluid's index of refraction, $\partial^2 n/\partial x^2$. The index of refraction is related to the fluid density by the following relationship:

Equation 2.3 $$n - 1 = k\rho$$

The Gladstone-Dale coefficient, k, is about 0.23 cm^3/g for air at standard conditions (Settles, 2001). For a perfect gas, the fluid density is directly related to the static pressure, and inversely related to the static temperature of the flow. Shadowgraphy lends itself well to the visualization of shock waves, which produce a step change in flow properties across the shock front.

A shadowgraphy system is implemented in the Virginia Tech Transonic Cascade Wind Tunnel as shown in Figure 2.8. The light source is a Xenon Corporation Model 4378 Nanopulser, which produces a very short-duration pulse of high intensity light by creating a spark between two electrodes. The Nanopulser is placed at the focal point of a parabolic mirror, which generates a light column. This light column is then focused to pass through the cascade test section parallel to the blade surfaces. A Polaroid 545 Pro camera loaded with 3000 speed film is placed on the other side of the test section, within the illuminated region. The Nanopulser is triggered when the shock passes a Kulite pressure transducer mounted on the test section wall. The placing of this Kulite determines the location of the shock in the resulting shadowgraph image.

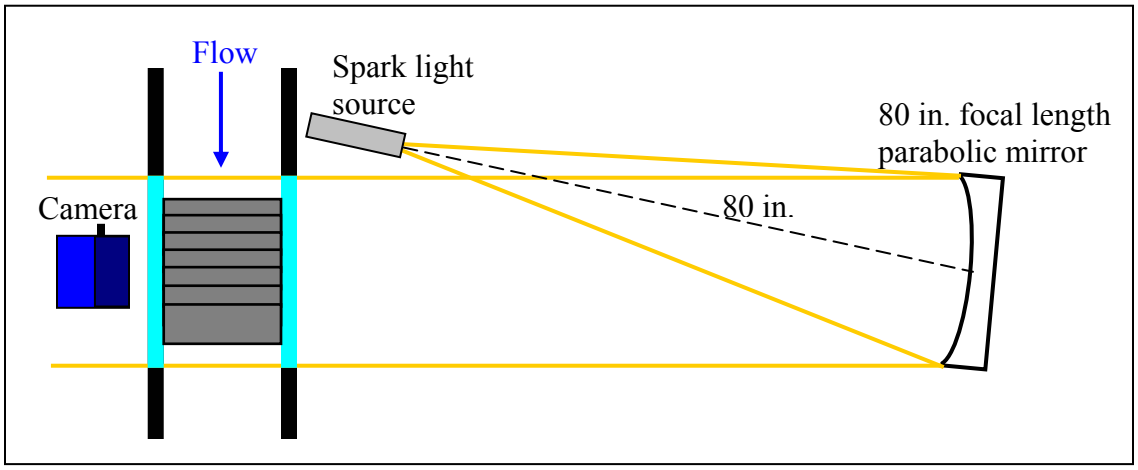

Figure 2.8: Schematic of shadowgraphy system.

2.7: Digital Particle Image Velocimetry System

The DPIV capabilities for this project were provided by Dr. Jordi Estevadeordal of Innovative Scientific Solutions, Inc. (ISSI). ISSI is based in Dayton, OH and specializes in optical diagnostic techniques for the aerospace industry.

Like many flow visualization methods, DPIV involves the injection of small seed particles into the flow. Suitable particles include TiO_2, Al_2O_3, cornstarch, and talcum powder. The seed particles for the tests discussed in this report were injected through a perforated tube upstream of the stator cascade using pressurized air. Two frequency-doubled Nd:YAG lasers are used for illumination. The beams are sent through sheet-forming optics housed within a glass tube that protrudes into the test section. The resulting laser sheet is less than a millimeter thick and exposes all particles within a two-dimensional slice of the flow field. Two laser pulses are generated in rapid succession (2μs apart for these tests) and an ES1.0 Kodak CCD camera captures the resulting image pair (Estevadeordal et al., 2002). Figure 2.9 shows the DPIV setup for this project.

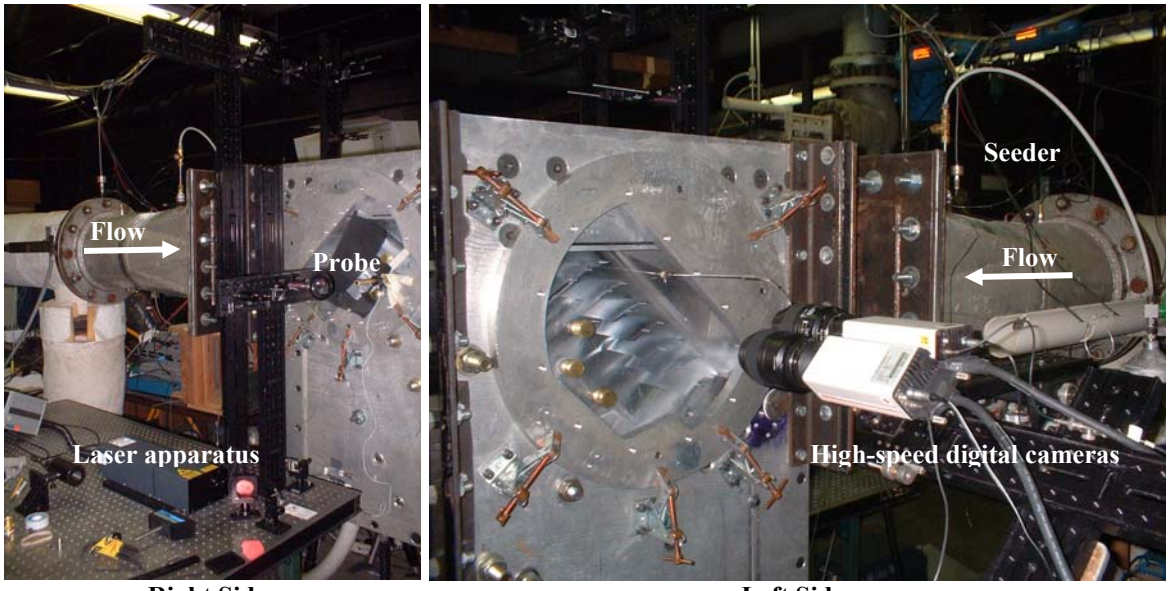

Figure 2.9: DPIV equipment at the Virginia Tech Transonic Cascade Wind Tunnel.

For runs involving a moving shock, the laser and camera are triggered from a wall-mounted Kulite pressure transducer. The sudden pressure rise across the moving shock causes the output voltage from the transducer to exceed a predetermined threshold,

initiating the LeCroy A/D converter to send a TTL trigger signal to the DPIV electronics. By placing the Kulite at different wall locations, images for different shock locations may be captured.

After the image pair is captured, proprietary ISSI software is used to calculate velocity vectors. The first image of the pair is given a red hue, and the second image is given a green hue. The two images are then overlaid, resulting in an image like the one seen in Figure 2.10. The software divides the image up into correlation windows and generates vectors based on the direction and distance that the average particle within each window traveled. In this manner, precise velocity vector fields were determined for the various shock strengths and locations in these experiments.

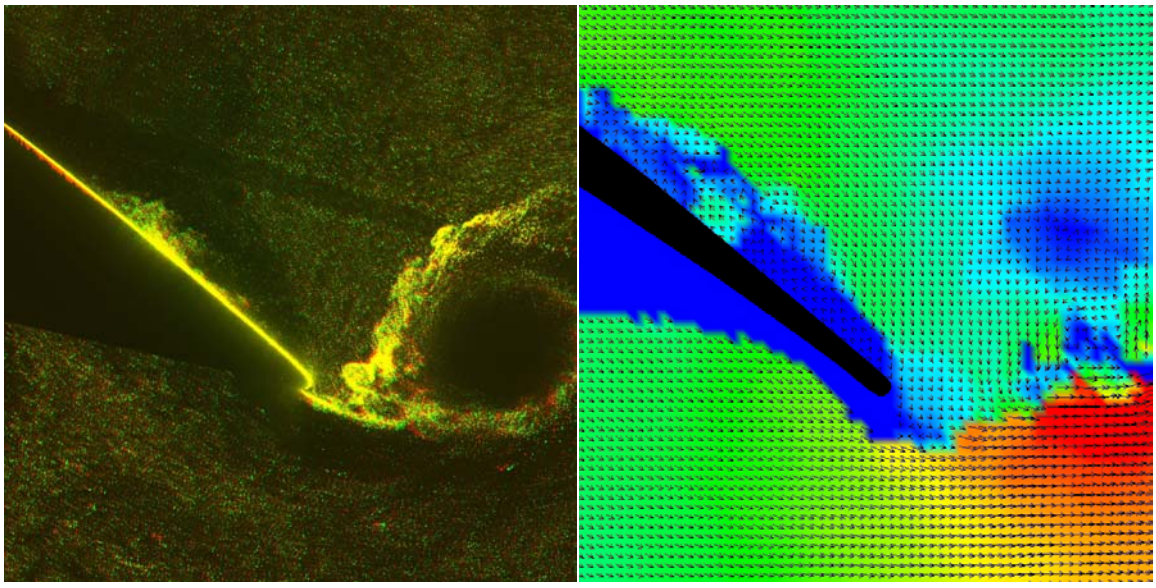

Figure 2.10: Red-green overlay of sequential DPIV images (left) and resulting velocity vector field (right).

The current DPIV system has its drawbacks; primarily the inability to generate velocity correlations near the blade surface. One reason for this is the relative lack of seed particles in the blade surface boundary layer. Despite the blades being painted flat black, there is also a small region of glare due to laser reflection on the blade suction surface. The glare dominates the correlation windows nearest to the blade surface, producing meaningless vectors. In addition, it is impossible for a single laser sheet to illuminate both the pressure and suction surfaces of the blade, so there is a shadow region below the blade pressure surface where no seed particles are illuminated.

Chapter 3.0: Steady Results

3.1: Wake Stagnation Pressure Losses

The primary source of steady losses for any subsonic compressor cascade is the stagnation pressure deficit in the blade wakes. While a certain degree of wake loss is unavoidable, stator rows are designed to minimize wake size at design incidence. The stagnation pressure loss at any point in the flow downstream of the stator is quantified by the local total pressure loss coefficient, ω:

Equation 3.1

$$\omega = \frac{P_{01} - P_{02}}{P_{01} - \overline{P_1}}$$

Data were gathered by traversing the angle probe through two full pitches while operating the tunnel at the design inlet Mach number of 0.65. All upstream and downstream pressure measurements were logged. The experiments were repeated for five different cascade incidence angles: design incidence (inlet flow parallel to the blade inlet camber line), ±2°, and ±5°. The local total pressure loss coefficient distribution downstream of the center blade in the cascade at the five different incidence angles may be seen in Figure 3.1. All wake data were gathered at 45% chord downstream of the TE.

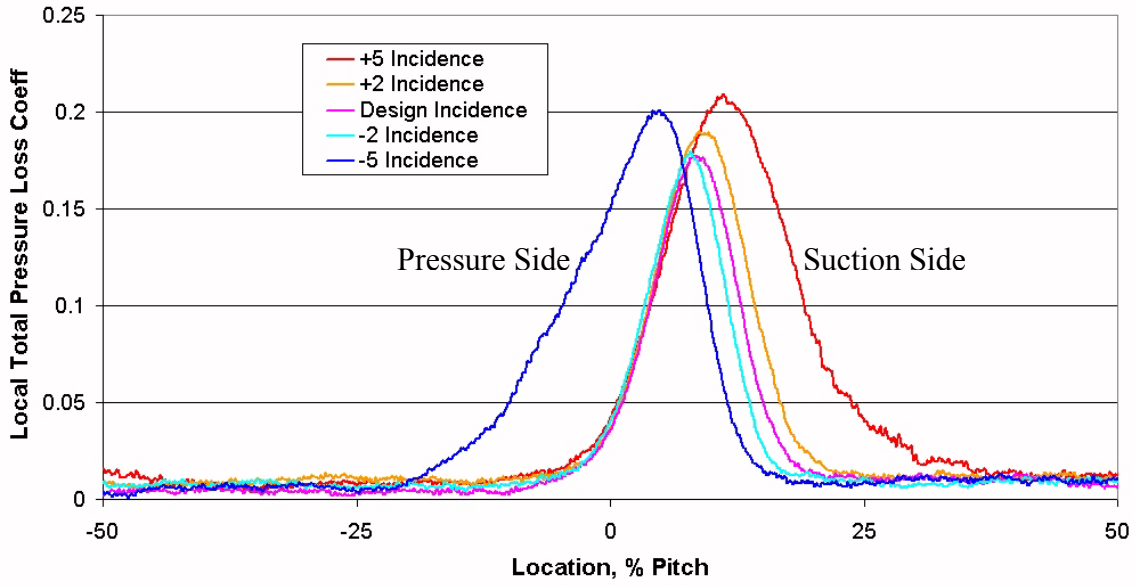

Figure 3.1: Stator wake profiles for various incidence angles.

3.2: Influence of Incidence Angle on Losses

The local total pressure loss coefficient distributions of Figure 3.1 may be averaged over one blade pitch to yield the area-averaged total pressure loss coefficient:

Equation 3.2

$$\overline{\omega} = \frac{\sum_{i=1}^{i=n} \omega_i \Delta y}{y}$$

where y is the pitch, Δy is the spatial increment between data points, and n is the number of data points in the sample. The area-averaged total pressure loss coefficient is plotted versus incidence angle in Figure 3.2.

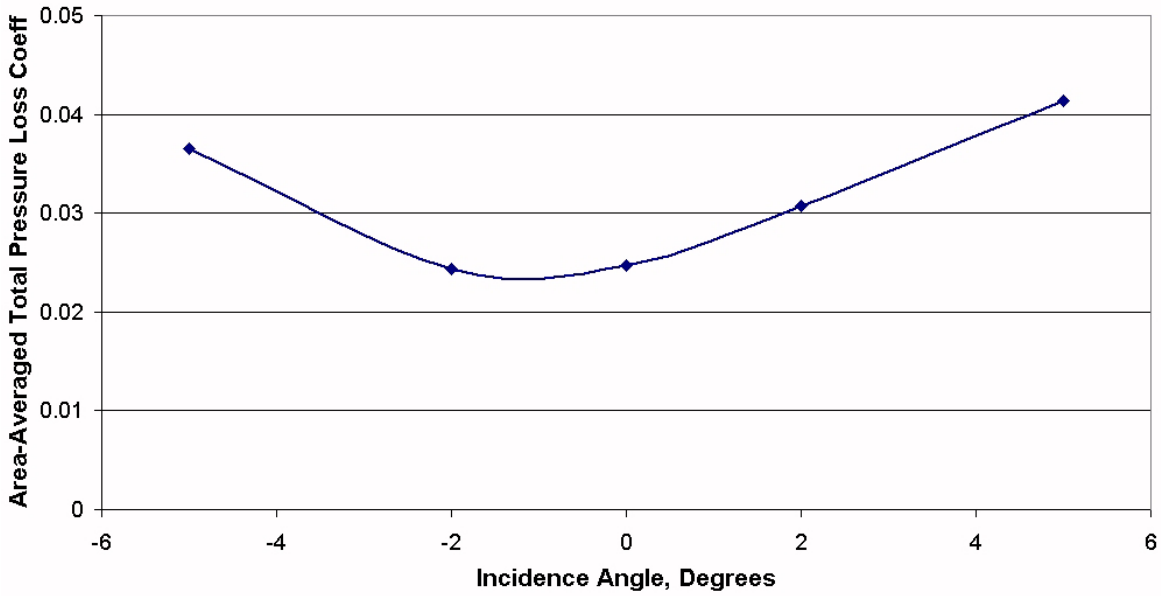

Figure 3.2: Area-averaged total pressure loss coefficient versus incidence angle.

As expected, the lowest losses occur near the design incidence, and increase as the incidence angle deviates from design. The loss coefficient at design incidence, 0.025, is relatively low for a stator cascade in this particular facility. One explanation for this is that the stators used in the experiment are not highly loaded, and therefore do not experience suction surface boundary layer separation. The overall low losses, which occur near design incidence, are a very good indication that the stator cascade is operating properly.

3.3: Stator Exit Flow Angle

In an axial compressor, the stator rows serve two primary purposes: to provide diffusion and to turn the flow so that it enters the downstream rotor row at the correct angle. If the flow is turned to be uniformly tangent to the exit camber line, the blade row geometry dictates that the correct static pressure rise has also been achieved. Therefore, the exit flow angle from the stator row is of primary importance in determining whether the cascade is operating properly.

The downstream angle probe was aligned with the stator exit camber line so that the calculated flow angle would correspond to the flow deviation angle. The flow angle was calculated from the three angle probe pressure measurements using the MATLAB code shown in Appendix A. Figure 3.3 shows the deviation angle distribution along one pitch directly downstream from the center blade in the cascade for the five different incidence angles. The flow angle uncertainty in the freestream is ±½°. However, due to the large spacing of the probe ports relative to the wake thickness, the uncertainty in the wake region is somewhat higher. The data has been shifted to place all three probe ports at the same location for a given instant in time, but wake unsteadiness still leads to a larger error in this region.

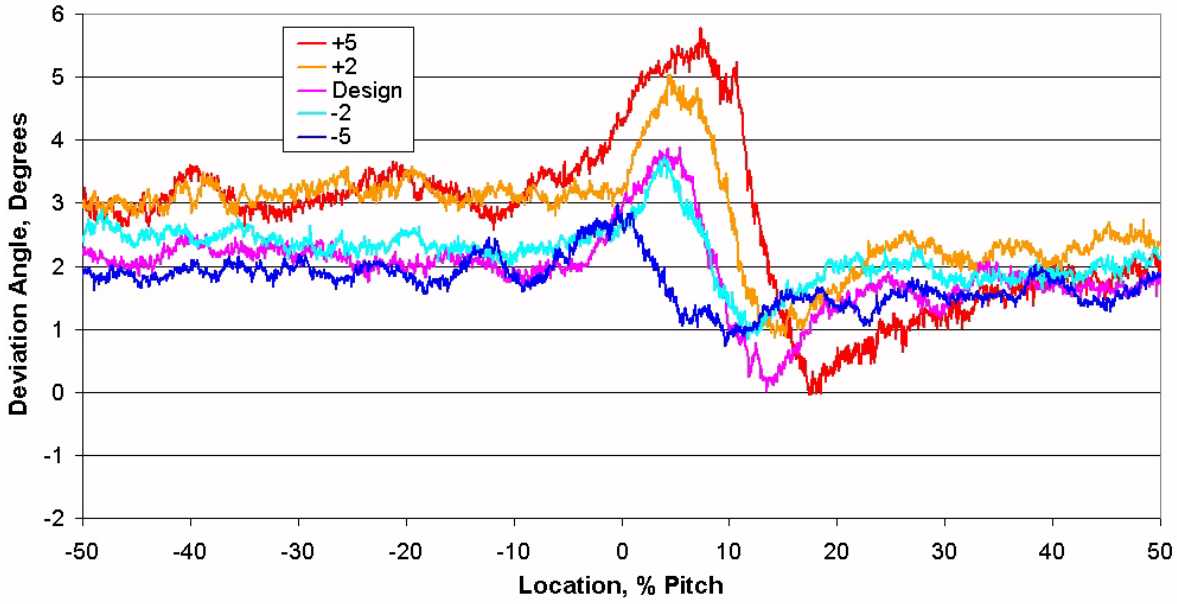

Figure 3.3: Deviation angle distribution for various incidence angles.

The average deviation angle for all five incidence angles is less than 3°, which is further evidence that the stator cascade is closely duplicating the design compressor conditions. The viscous nature of the stator flow field prevents the average flow deviation from reaching zero, but a 3° deviation is within acceptable limits.

3.4: Blade Surface Static Pressure Distribution

Downstream measurements provide valuable indications of the overall performance of the stator row, but they do not offer any details on the flow field within the blade passage. In order to gain a deeper understanding of the passage flow, two adjacent blades in the cascade were replaced with the blades instrumented to measure the blade surface static distribution. The blade surface static pressure measurements are of little value without some means of extending the pressure at the blade surface into the freestream, so it is necessary to consult the following analysis by Schetz (1993).

For flow over a body with modest curvature (such as the stator blade in the current work), the development of a thin viscous layer may be assumed. Since the layer is thin, streamlines in the boundary layer must all be roughly parallel to the blade surface and therefore have modest curvature as well. The static pressure gradient normal to the streamlines is related to the flow velocity and streamline radius of curvature by the following equation:

Equation 3.3

$$\frac{\partial p}{\partial n} = \frac{\rho V^2}{R_C}$$

Evaluating Equation 3.3 for a few typical values of R_C, V, and ρ encountered in this experiment yielded static pressure gradients on the order of 1 kPa/cm. This static pressure gradient is negligible when compared to the relative thickness of the blade surface boundary layers. Therefore, the measured blade surface static pressure distributions may be considered valid for the freestream flow immediately outside the boundary layer.

The blade surface static pressure was measured at twelve locations ranging from about 10% chord to 90% chord along the suction surface of the center blade in the

cascade and along the pressure surface of the blade above it. The measured static pressure is best presented in the form of an isentropic surface Mach number, which is calculated in the same manner as the inlet Mach number of Equation 2.2, but with P_1 replaced with the local static pressure on the blade surface. There is no stagnation pressure loss under the isentropic assumption, so the inlet stagnation pressure is used in the isentropic Mach number calculations. Figure 3.4 is a plot of the isentropic surface Mach number distribution for design incidence at the design inlet Mach number of 0.65.

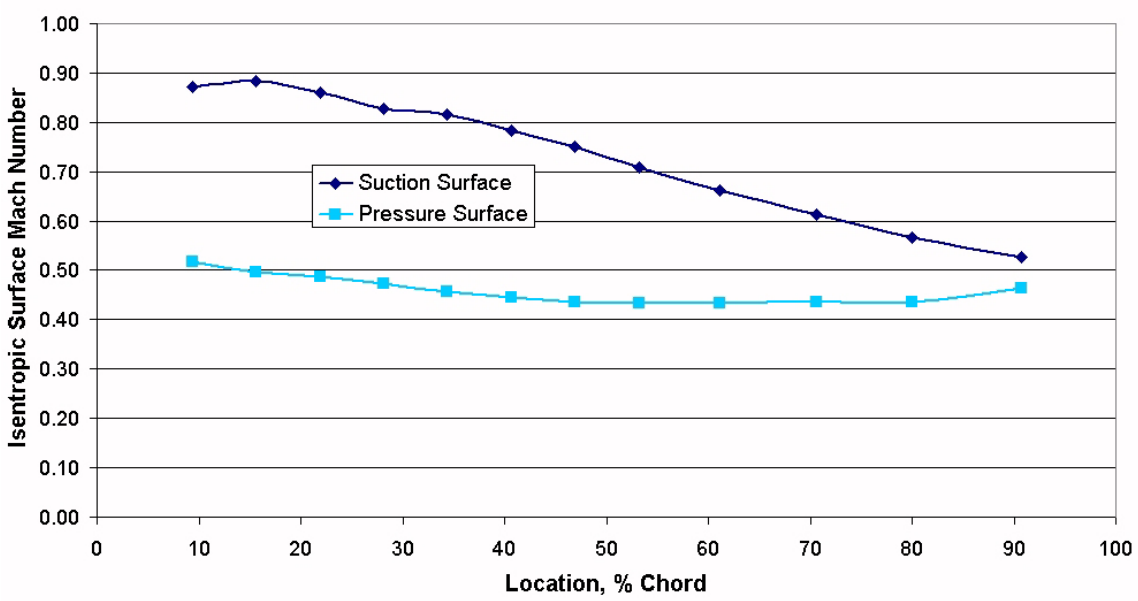

Figure 3.4: Isentropic Mach number distribution along blade surface at design incidence.

On both the pressure and suction surfaces, the static pressure distribution is very smooth and continuous. The isentropic Mach number remains subsonic along the entire suction surface, which indicates that there are no losses due to stationary shocks. Data were also gathered for ±5° incidence angles, and isentropic surface Mach number distributions for these off-design incidence angles may be seen in Appendix B.

Chapter 4.0: Unsteady Results

4.1: Shock Strength and Orientation

Matching the conditions of the moving shock in the cascade to the rotor bow shock in the actual compressor was the first task for the unsteady tests. Data from the actual compressor indicated that the shock should be oriented 37° from axial and have a shock strength (given as Ps_2/Ps_1) of 1.47. However, the shock strength decays as the shock expands through the cascade, so the desired shock strength may only be achieved at one location. The trailing edge of the center blade in the cascade was chosen to be the location at which the shock strength would be measured. Figure 4.1 compares the desired shock orientation to a shadowgraph image of the actual shock wave passing the center blade in the cascade. Note that the actual shock orientation matches the desired orientation very well.

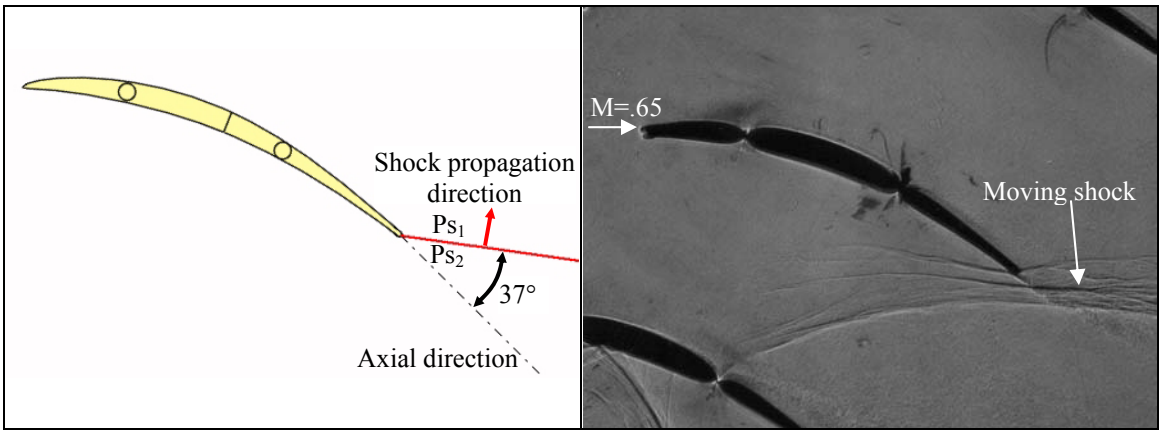

Figure 4.1: Desired shock orientation (left) and a shadowgraph of the actual shock in the cascade (right).

The wall-mounted Kulite pressure transducers were used both to measure the shock strength and verify the shock angle. Kulite locations 1 and 2 from Figure 2.7 are positioned along a line 37° from axial, so a properly oriented shock would produce a simultaneous pressure rise at both transducers. After some initial iteration on the shock shaper angle within the cascade, a nearly simultaneous pressure rise at Kulite locations 1 and 2 was achieved. Figure 4.2 shows the wall static pressure at these two locations during the shock-passing event.

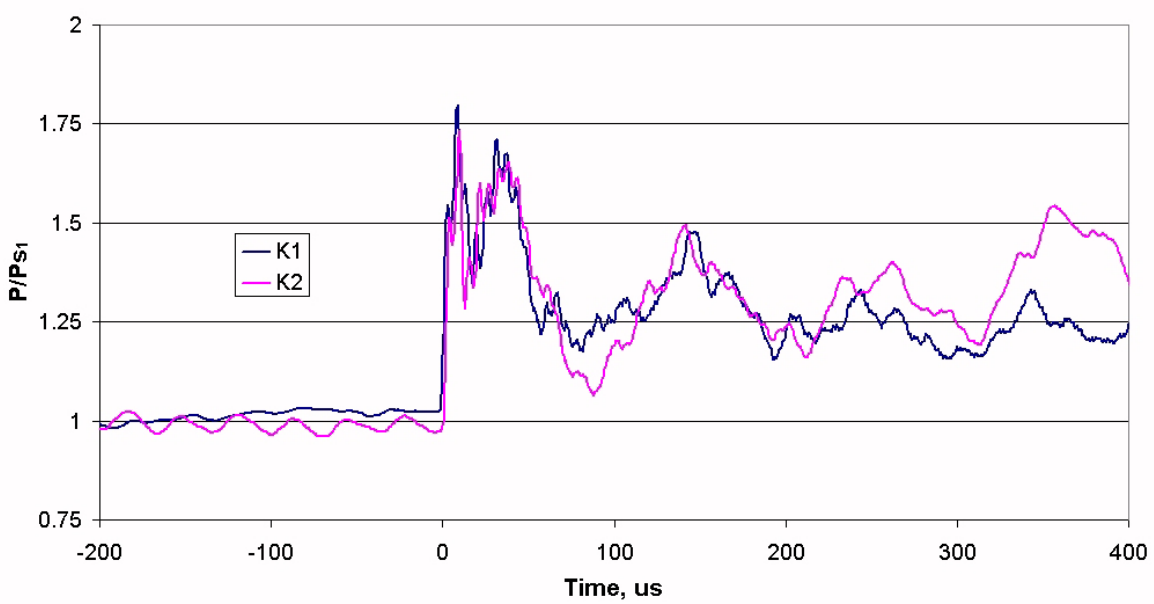

Figure 4.2: Wall static pressure at Kulite locations 1 and 2 during the shock-passing event (nominal shock strength=1.76). M=0.65.

Matching the shock strength to the desired value of 1.47 proved to be more difficult than matching the shock angle. Imperfections in the Mylar diaphragm material caused significant variation in the rupture pressure, and thus shock strength, from run-to-run. Also, diaphragm material was only available in two thicknesses (.003 in. and .007 in.), and stacking diaphragms increased the rupture pressure variability even more. Therefore, three different diaphragm thicknesses producing a wide range of shock strengths that encompassed the desired value of 1.47 were used for later experiments. Table 4.1 outlines the average shock strengths for the three diaphragm thicknesses and the run-to-run standard deviation of the shock strength. Ps_1 in the shock strength calculation was set equal to the ambient pressure of about 13.7 psia, and Ps_2 was taken to be the maximum wall static pressure at Kulite location 2 during the shock-passing event.

Table 4.1: Shock strengths for different diaphragm thicknesses.

Diaphragm Thickness (inches)	Ps_2/Ps_1	Standard Deviation
.003	1.42	2.3%
.007	1.76	6.3%
.014 (two .007 in. stacked)	2.10	9.7%

4.2: Shadowgraph Shock Progression

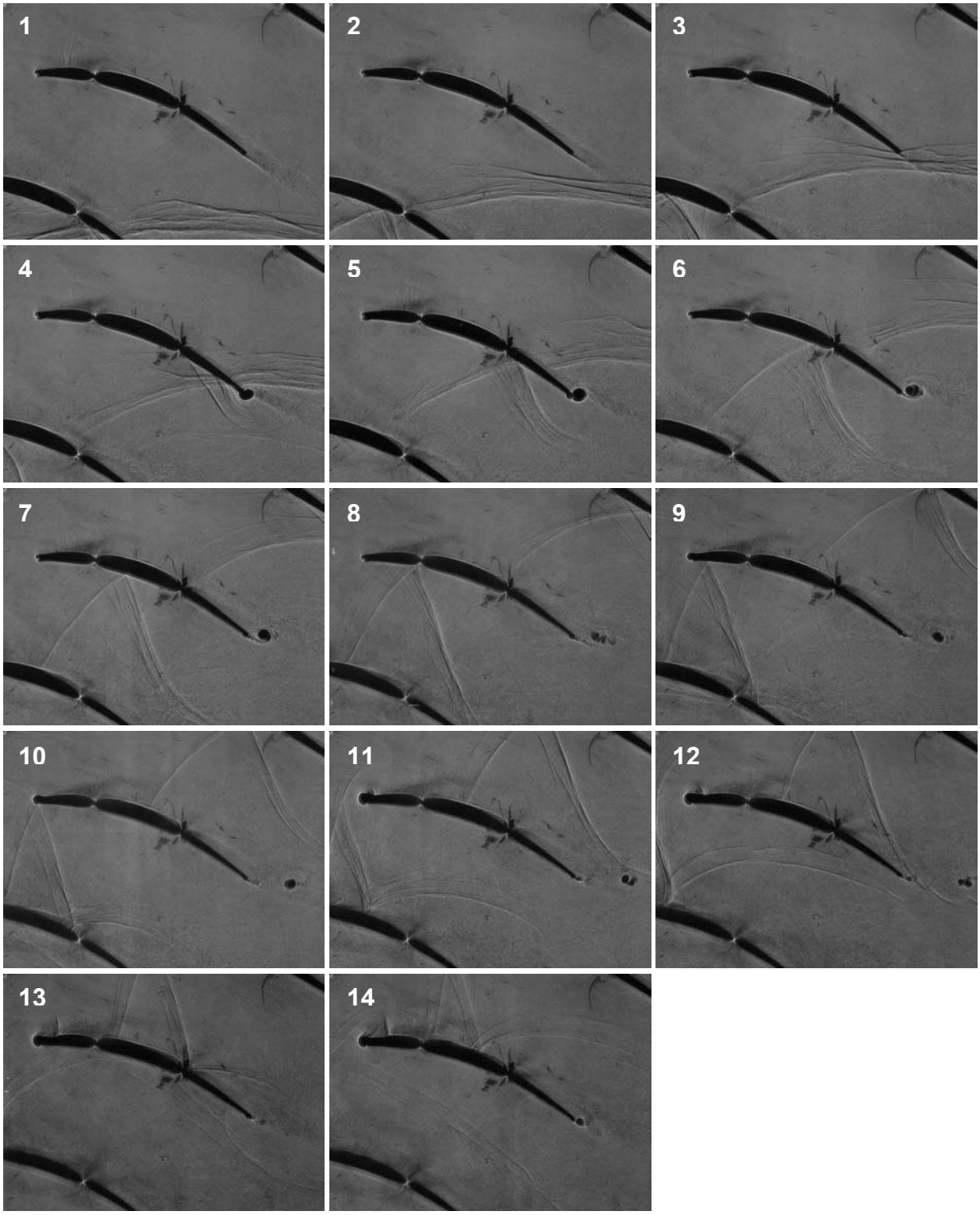

Figure 4.3: Shadowgraph shock progression for 1.76 shock strength.

The shadowgraph images of Figure 4.3 were taken from different runs (due to limitations with the photography equipment), but each image was triggered from a different wall Kulite location. The trigger locations are spaced ½ in. apart and form a line parallel to the cascade angle. This line of trigger locations is placed just far enough downstream from the trailing edge to not appear in the shadowgraph images, and may be seen in the test section window of Figure 2.1. Although the trigger locations are equally spaced, the shock propagation speed decreases the further the shock is from the shock shaper exit, so the actual time delay between each successive image in Figure 4.3 increases slightly and is difficult to estimate.

The most significant flow feature present in Figure 4.3 is the vortex that forms as the shock passes the stator trailing edge in image 4. This vortex grows slightly as it propagates downstream, reaching its peak size in image 6, and is still intact as it leaves the image region. The shadowgraph images show that the vortex causes the blade wake to shift upwards. The direction of vortex propagation is also of interest; rather than traveling tangent to the stator exit camber line (the design flow direction), the vortex seems to propagate along a line about 30° above the design flow direction.

Not surprisingly, shadowgraphs from this experiment support the phenomenon that Gorrell et al. (2002) observed whereby the rotor bow shock turns as it passes the stator trailing edge and propagates upstream as a normal shock. The shock has an angle relative to the blade suction surface of about 27° just as it is passing the trailing edge in image 4, but has turned to be nearly 90° from the blade surface by image 10. A series of reflected shocks also propagate upstream behind the original shock front, but these shocks have a lesser angle relative to the blade suction surface.

4.3: Digital Particle Image Velocimetry Results

4.3.1: DPIV Vortex Progression

DPIV data were gathered for various times in the shock-passing event. In order to achieve better resolution of the trailing edge vortex, the DPIV window only encompassed one square inch centered on the trailing edge of the center blade in the cascade. Figure 4.4 shows a series of shadowgraph images during the shock-passing event and their corresponding DPIV velocity vector fields.

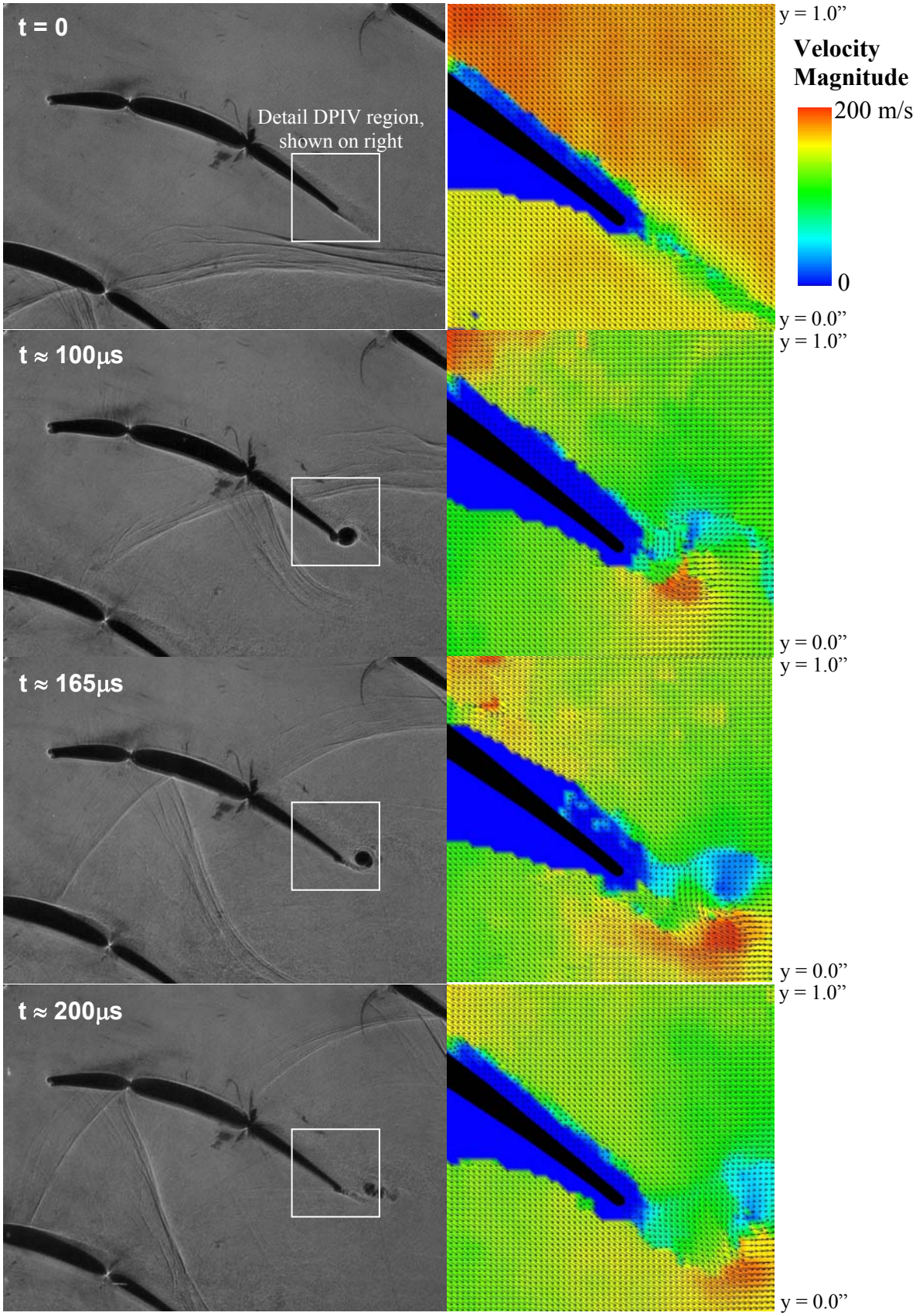

Figure 4.4: Shadowgraph (left) and DPIV (right) images of the trailing edge vortex created by the moving shock (shock strength=1.76).

There are several important flow features present in Figure 4.4. First, note the overall reduction in freestream velocity magnitude due to the shock-passing event. This drop in velocity magnitude is due to the superposition of the upstream-facing induced velocity field behind the moving shock with the unperturbed velocity field. The immediate nature of the velocity reduction across the moving shock may be seen in the DPIV image at t≈100μs. The shock appears in the upper left corner of this image as a distinct velocity magnitude discontinuity.

DPIV also provides significantly more detail about the vortex flow field than the shadowgraphs, which merely show the vortex size. It is clear from examining the velocity vectors in Figure 4.4 that the vortex rotates counter-clockwise in the reference frame of the DPIV images. The result of this counter-clockwise rotation combined with the freestream flow to the right is a region of nearly zero velocity above a region of very high velocity. As the shadowgraphs also showed, the DPIV images show the vortex growing in size as it propagates downstream.

4.3.2: Effect of Shock Strength on the Trailing Edge Flow field

The trailing edge velocity field after the shock-passing event was captured for the three different shock strengths of Table 4.1. While a vortex clearly formed in each case, the size of the vortex proved to increase directly with shock strength. Figure 4.5 shows the trailing edge velocity vector fields for the three different shock strengths at t≈100μs.

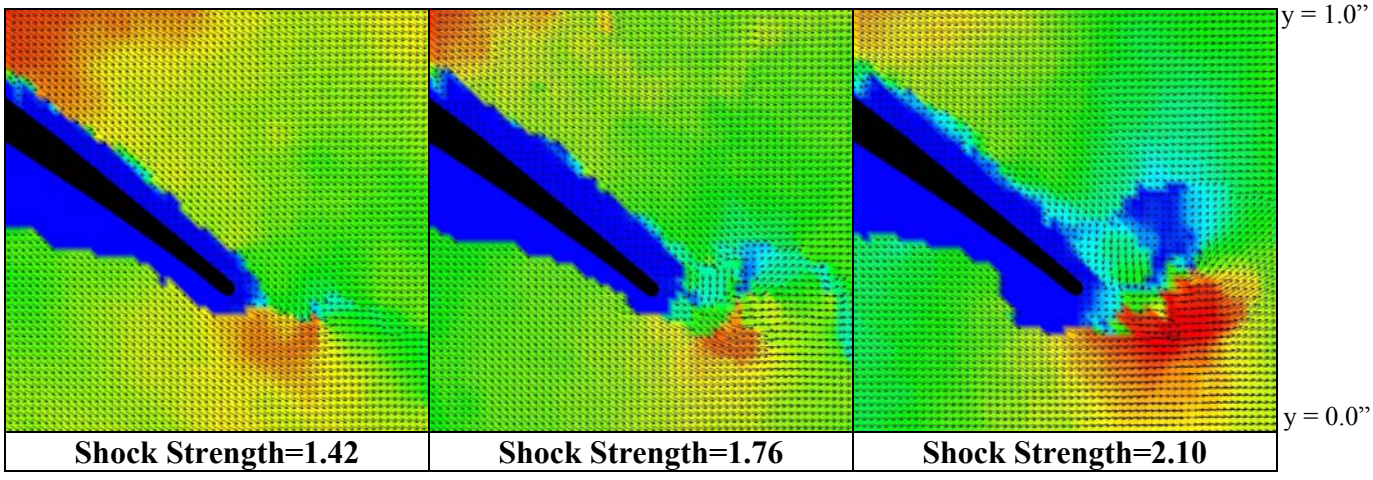

Figure 4.5: Trailing edge velocity vector fields for three different shock strengths at t≈100μs.

There are a few important trends visible in the images of Figure 4.5. Primarily, the disparity between the velocity magnitudes in the vortex compared to the freestream increases with greater shock strength. This means that in addition to increased vortex size, greater shock strengths also produce a faster-spinning vortex. Another consequence of increased shock strength is a vortex whose influence extends further upstream. Note for the 2.10 shock strength, the vortex seems to curl back around to the suction surface near the trailing edge, whereas the vortex influence is limited to downstream of the trailing edge for the lower shock strengths.

4.4: Loss Estimation

4.4.1: Passage Blockage

From Figure 4.4, the vortex travels approximately ¼ of an inch between t≈100μs and t≈200μs, which corresponds to a propagation velocity of about 60 m/s. This means the vortex travels downstream at roughly half the local freestream velocity, causing the freestream flow to bypass the slower-moving vortex. In this manner, the vortex acts as a passage blockage.

The best way to qualitatively see the effects of the passage blockage due to the vortex is to plot streamlines for the DPIV solutions. The stream function, ψ, is defined as follows for incompressible flow:

Equation 4.1 $$d\psi = -vdx + udy$$

where lines of constant ψ represent streamlines (Sabersky et al., 1999). The only information contained in the DPIV solutions are the x and y components of velocity at 3600 discrete locations, but this is sufficient to calculate streamlines. The unsteady nature of the trailing edge flow field means that the calculated streamlines are instantaneous and do not represent *pathlines* that a specific particle would take through the flow during the unsteady vortex-formation event. However, they do provide a suitable representation of the flow field at a specific instant in time.

Figure 4.6 shows a set of streamlines near the blade trailing edge for four cases; steady flow and the unsteady flow field at t≈100μs for each of the three shock strengths.

The streamlines were used to approximate an effective blockage size, which is represented by a red circle. Note that the effective blockage diameter is directly proportional to the shock strength. It is possible that the blockage also led to boundary layer separation on the blade suction surface, but the DPIV drawbacks discussed in Section 2.7 prevented the capture of any meaningful velocity vectors in this region.

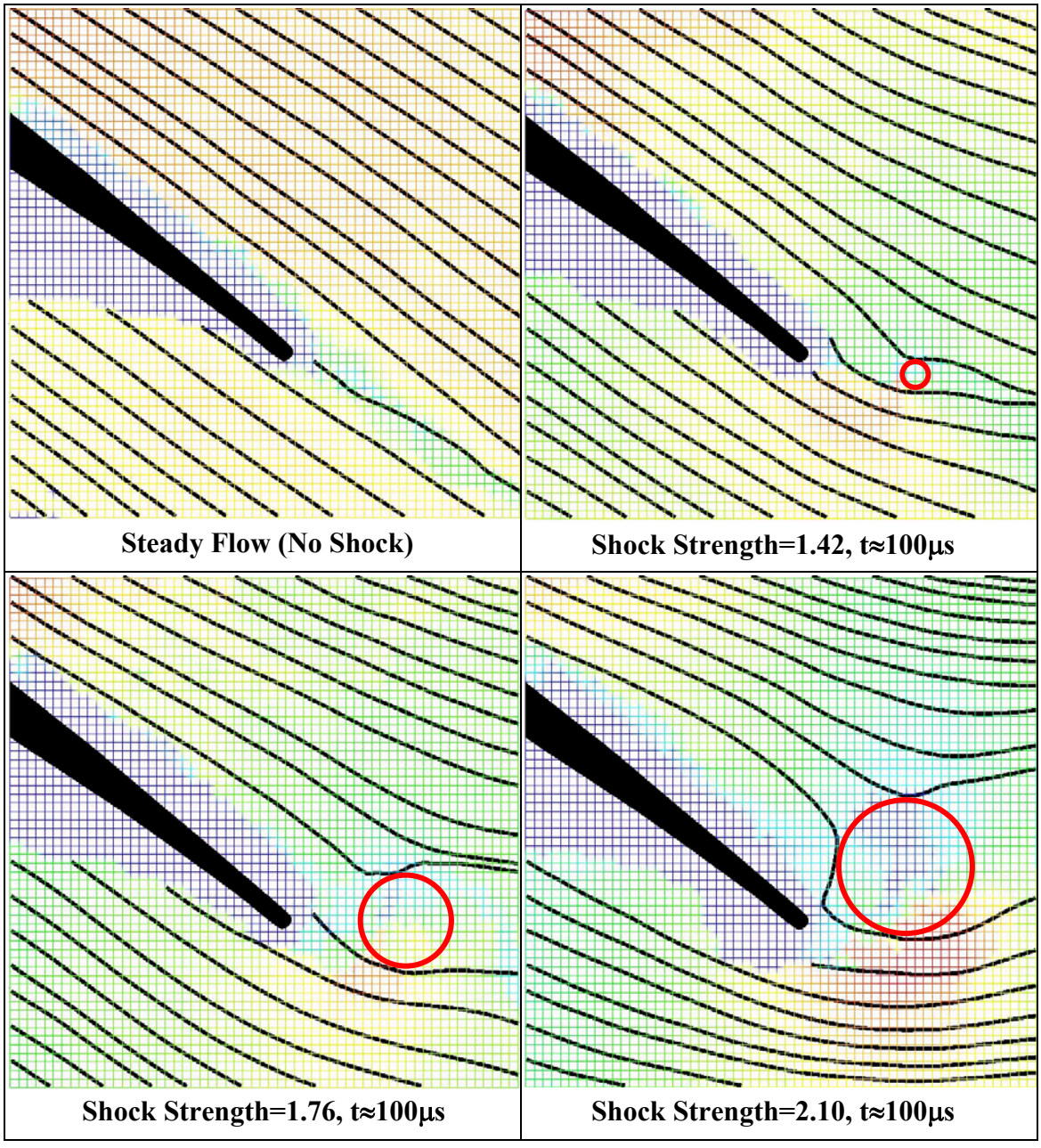

Figure 4.6: Instantaneous streamlines for steady flow and three different shock strengths and corresponding effective blockage.

The corresponding blockage as a percentage of the cascade pitch is shown in Table 4.2. The relationship between shock strength and passage blockage due to the vortex is directly related. Within an actual gas turbine engine, increased flow path blockage leads to reduced mass flow rate (and therefore reduced thrust), so compressor blockage on the order of 3-15% would have the potential to cause serious problems.

Table 4.2: Effective vortex blockage versus shock strength at t≈100μs.

Shock Strength	Effective Vortex Blockage, % Pitch
1.42	2.9%
1.76	10.0%
2.10	14.3%

4.4.2: Flow Angle Deviation due to the Shock-Passing Event

While not a loss mechanism itself, turning of the stator exit flow away from its design exit flow angle could lead to separation losses in the downstream rotor. The DPIV data were used to quantify the level of exit flow deviation (from the design exit flow angle) during the shock-passing event. Figure 4.7 shows the deviation angle distributions along the right edges of the four DPIV velocity fields of Figure 4.4, which are approximately 17% chord downstream from the trailing edge.

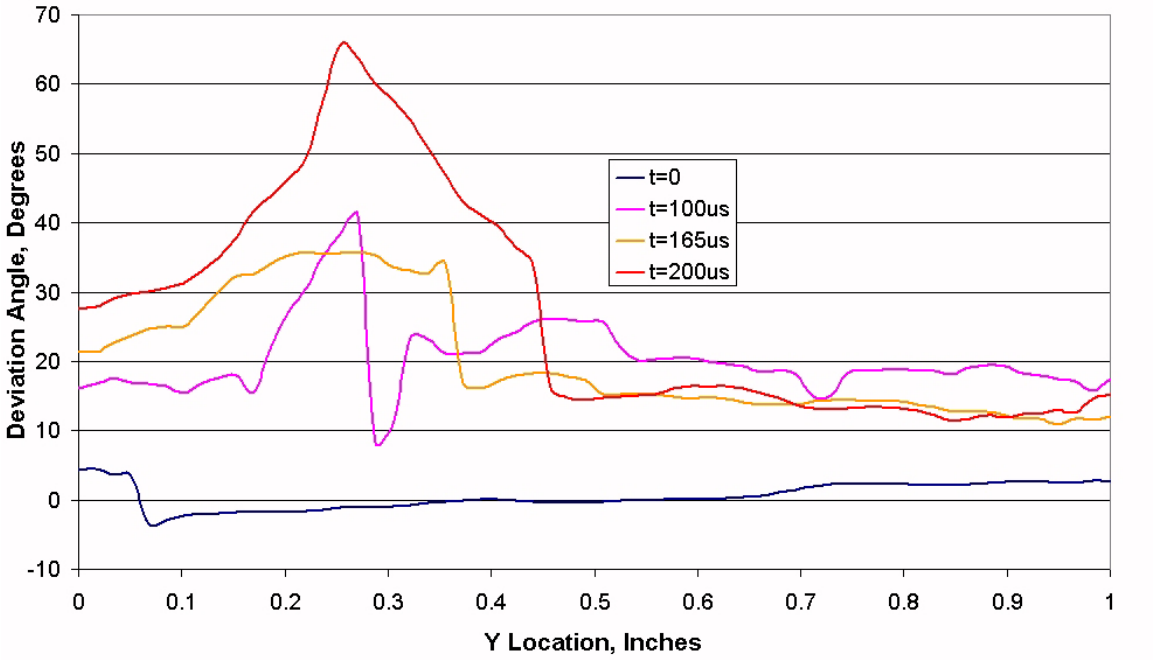

Figure 4.7: Deviation angle distribution along the right edges of the DPIV images from Figure 4.4 (shock strength=1.76).

Not unexpectedly, the deviation angle is relatively constant near zero before the shock arrives (t=0). However, after the shock passes the trailing edge, the deviation angle distribution downstream of the stator increases drastically. In the freestream, the deviation angle increases roughly 10-20° due to the flow turning induced directly by the shock. This freestream deviation is expected and is counteracted in the actual compressor by a series of expansion waves behind the rotor bow shock that turn the flow back towards its design angle. However, the extensive deviation near the vortex-influenced region (y=0 to y=0.5 in.) is an unexpected consequence of the vortex formation event. Both the maximum and overall deviation in this region increase as the vortex propagates downstream. The blade period in the actual compressor is 183μs, so the vortex-induced flow deviation would be reaching its maximum as the next shock passed and formed another vortex.

The influence of shock strength on the deviation angle distribution was also investigated. Figure 4.8 shows the deviation angle distributions along the right edge for the three DPIV velocity fields of Figure 4.5, which were measured at roughly the same time in the shock-passing event (t≈100μs). Note that both the overall and maximum deviations are directly related to the shock strength.

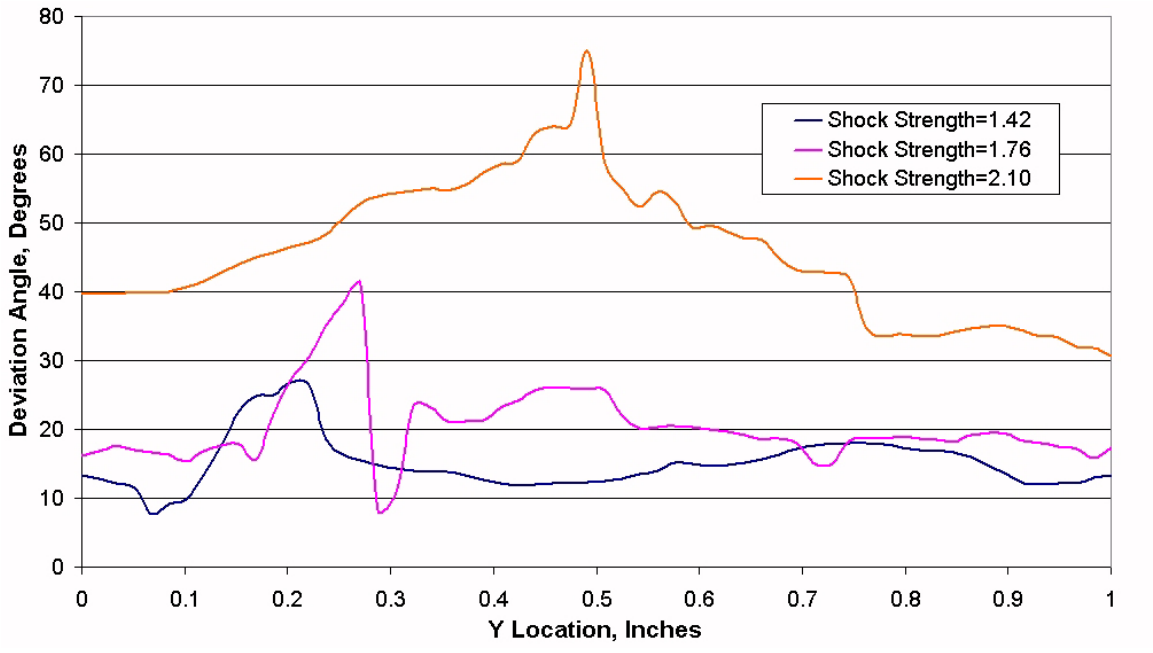

Figure 4.8: Deviation angle distribution along the right edges of the DPIV images from Figure 4.5 (t≈100μs).

4.4.3: Vorticity Losses

The DPIV data only provide velocity information, so an analytical approach must be taken to estimate the stagnation pressure loss due to the trailing edge vortex. The relationship between vorticity, ζ, and the entropy gradient normal to the streamline is given by Crocco's Theorem:

Equation 4.2 $$T\frac{dS}{dn} = \frac{dh_0}{dn} + u\zeta$$

While the stagnation enthalpy, h_0, is not constant across the shock, h_0 may be considered constant for the trailing edge flow field after the shock passes. Under the assumption of constant stagnation enthalpy, Crocco's Theorem takes the follow form:

Equation 4.3 $$\zeta = \frac{T}{u}\frac{dS}{dn} = -\frac{RT_0}{uP_0}\frac{dP_0}{dn}$$ (Liepmann and Roshko, 1967)

where the vorticity for the two-dimensional DPIV flow field is defined by Equation 4.10.

Equation 4.4 $$\zeta = \frac{\partial v}{\partial x} - \frac{\partial u}{\partial y}$$

The local vorticity magnitudes at discrete locations in the DPIV velocity fields were calculated using the Fieldview software package. These local vorticity values were integrated over the entire region downstream of the trailing edge for the steady flow case and the three different shock strengths at $t \approx 100\mu s$. The result was an average vorticity magnitude value for the entire region, ζ_{AV}, as seen in Figure 4.11.

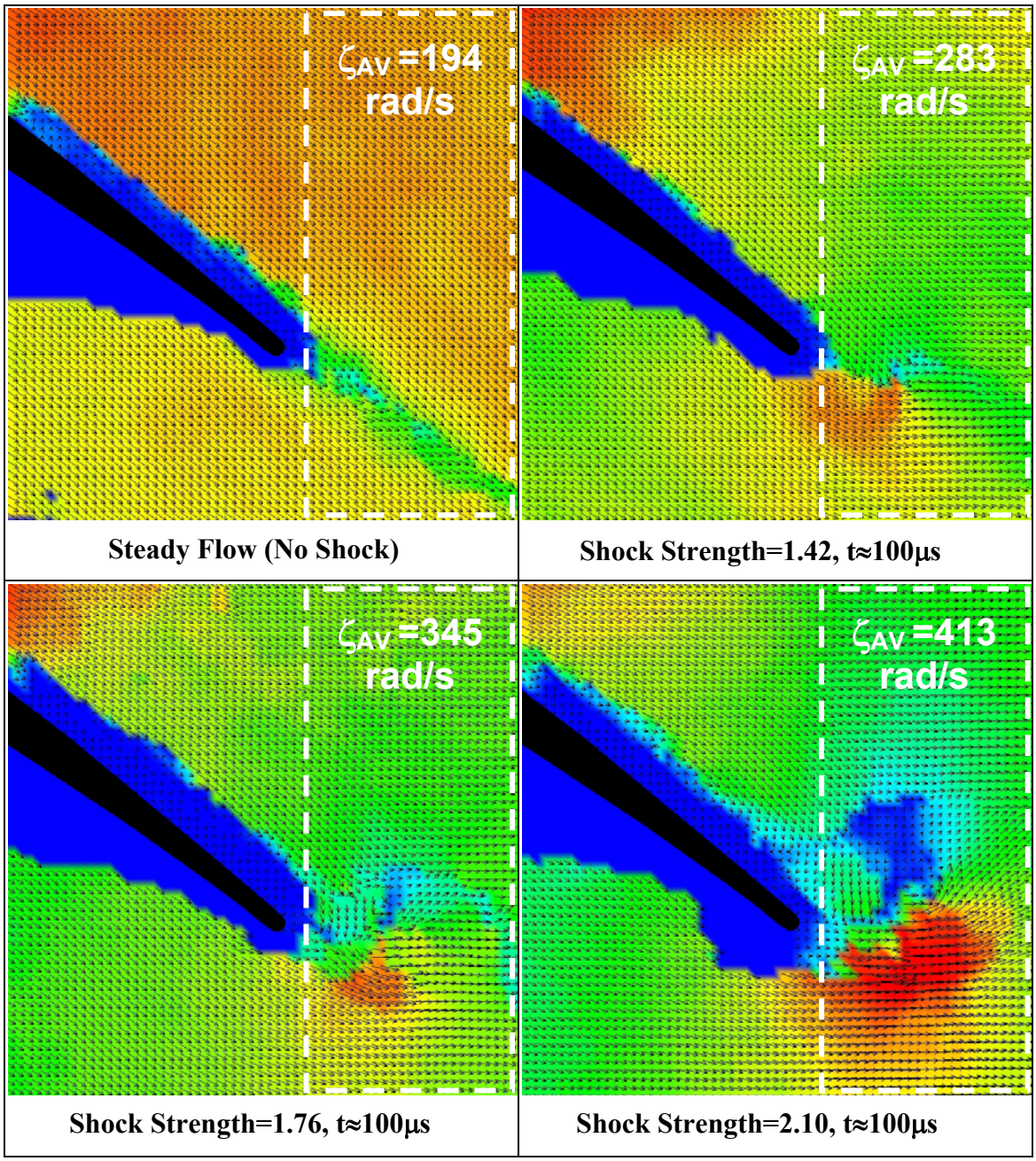

Figure 4.9: Average vorticity magnitudes in the trailing edge region for steady flow and three different shock strengths.

While insufficient information is available to accurately predict the exact stagnation pressure losses using the average vorticity magnitude values from Figure 4.9, some reasonable assumptions about the relative magnitude of the losses may be drawn. For steady flow, the average vorticity magnitude downstream of the trailing edge is 194 rad/s, with the momentum deficit in the wake contributing most to the average vorticity.

The corresponding area-averaged total pressure loss coefficient was measured to be 0.025 under steady operation at design incidence, as shown in section 3.2. If the stagnation pressure losses due to vorticity are considered to be the primary loss mechanism in this region of the flow, one may assume the losses to be directly proportional to the average vorticity in the stator exit flow region. Table 4.3 illustrates the estimated stagnation pressure loss due to the vortex for the three different shock strengths as a percentage of the steady loss value. For the highest shock strength, the estimated stagnation pressure loss due to vorticity is greater than the steady wake loss.

Table 4.3: Estimated vortex-induced stagnation pressure losses.

Shock Strength	**Estimated Vortex-Induced P_0 Losses over Steady P_0 Losses**
1.42	46%
1.76	78%
2.10	113%

4.4.4: Upstream-Propagating Shock Losses

The moving shock is initially oblique relative to the stator flow, but the shadowgraph images showed that the shock turns as it passes the trailing edge and eventually acts as an upstream-propagating normal shock. In order to estimate the stagnation pressure loss due to this shock, the states upstream and downstream of the shock front must be known. No unsteady pressure measurements were made within the blade passage, so the only available information of value is the absolute velocities upstream and downstream of the shock (from the DPIV results).

Figure 4.10 shows the first shadowgraph in the 1.76 shock strength sequence for which the shock has turned enough that it may be approximated as normal. The approximate velocities upstream and downstream of the shock front are also shown. The DPIV velocity field from which these values were obtained suffered from insufficient seeding in various regions (not including the shock region), so the DPIV image itself is not shown.

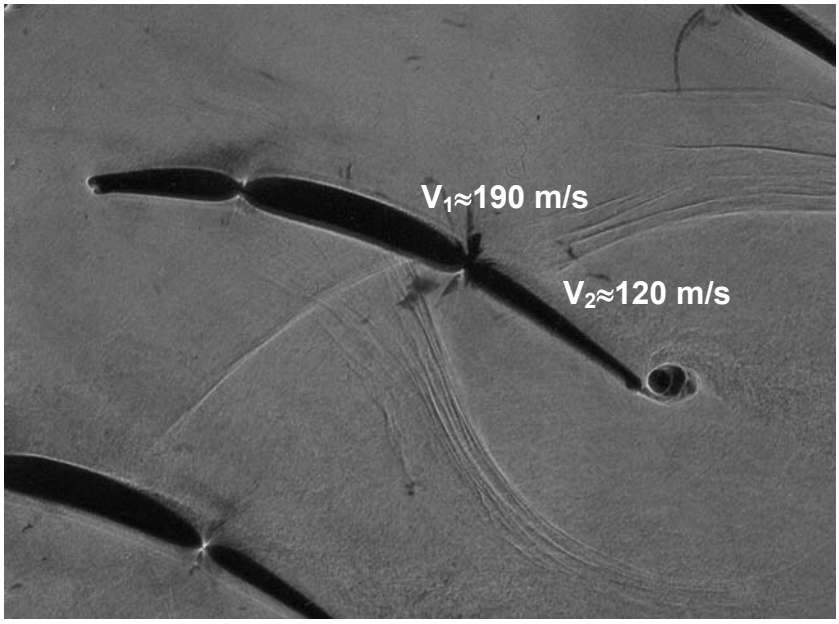

Figure 4.10: Shadowgraph image of upstream-propagating normal shock with velocity magnitudes on either side of the shock found from DPIV data (shock strength=1.76).

Although the static pressure ratio across the shock is approximately 1.76 at the trailing edge, the turning of the shock combined with natural decay as the wave expands through the cascade results in a reduced strength for the shock location of Figure 4.10. To estimate the static and stagnation pressure ratios across the shock, some simplifying assumptions must be made. The shock may be simplified as a moving normal shock with the characteristics shown in Figure 4.11.

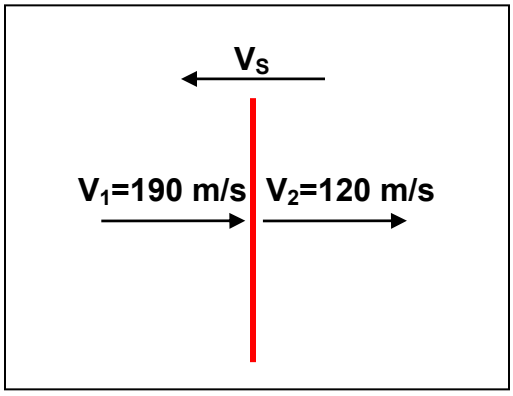

Figure 4.11: Schematic of simplified moving shock characteristics.

The static and stagnation pressure ratios across the shock are purely a function of the ratio of relative Mach numbers across the shock. The upstream and downstream Mach numbers relative to the moving shock reference frame are given in the following equations:

Equation 4.5
$$M_1 = \frac{V_1 + V_S}{\sqrt{\gamma R T_1}}$$

Equation 4.6
$$M_2 = \frac{V_2 + V_S}{\sqrt{\gamma R T_2}}$$

Combining the two equations yields:

Equation 4.7
$$\frac{M_2}{M_1} = \frac{V_2 + V_S}{V_1 + V_S}\sqrt{\frac{T_1}{T_2}}$$

Equation 4.5 gives the static pressure ratio across the shock under the assumption of adiabatic flow. All subsequent equations for this section are from Oosthuizen and Carscallen (1997).

Equation 4.8
$$\frac{T_1}{T_2} = \frac{\left(1 + \frac{\gamma - 1}{2} M_2^2\right)}{\left(1 + \frac{\gamma - 1}{2} M_1^2\right)}$$

Finally, the downstream Mach number relative to the moving shock is related to the upstream Mach number relative to the moving shock by the following equation:

Equation 4.9
$$M_2^2 = \frac{(\gamma - 1)M_1^2 + 2}{2\gamma M_1^2 - (\gamma - 1)}$$

Simultaneous solution of Equations 4.2 through 4.6 using the values of V_1 and V_2 given in Figure 4.10 and assuming T_1=20°C yields V_S=197 m/s, M_1=1.13, and M_2=0.89. The static pressure ratio across the shock may be calculated from these relative Mach

number values using Equation 4.10, which yields P_2/P_1=1.32. Therefore, the shock strength decayed from 1.76 to 1.32 as it turned normal to the passage flow.

Equation 4.10

$$\frac{P_2}{P_1} = \frac{1+\gamma M_1^2}{1+\gamma M_2^2}$$

The stagnation pressure ratio across this moving shock was found by evaluating Equation 2.2 using absolute Mach number values (rather than the relative Mach numbers used in the previous analysis) and the calculated static pressures upstream and downstream of the shock. The result was a 16% stagnation pressure *rise* across the shock. While this initially seems counter-intuitive, for a moving shock passing through non-stationary fluid, it is not unusual.

Within the actual compressor environment, the stagnation pressure rise may simply be seen as the downstream rotor doing work on the upstream stator flow field; the stagnation pressure increase does not come for 'free'. From a system perspective, the upstream-propagating shock would still generate a net stagnation pressure loss within the actual compressor. The extent of the net loss in stagnation pressure may be estimated by assuming the shock is stationary with M_1=1.13 and M_2=0.89. Consulting the normal shock tables for these Mach number values yields a stagnation pressure loss across the shock of 0.22%. While this may have a noticeable impact on actual compressor performance, it is clear that the stagnation pressure loss due to the upstream-propagating normal shock is not the primary unsteady loss mechanism.

Chapter 5.0: Conclusions and Recommendations

The first task for this project was to design and manufacture a linear cascade of stator blades to match the steady operating conditions for the first stage of a transonic compressor. Three types of steady measurements were taken while the cascade was operating at its design inlet Mach number of 0.65: stagnation pressure losses, exit flow angle, and the blade surface static pressure distribution. The area-averaged total pressure loss coefficient was found to be only 0.025 at the design incidence of 0º, and increased as the incidence angle deviated from design. Exit flow angle measurements revealed that the average deviation angle was less than 3º for the entire range of incidence angles that were tested. Finally, the blade surface static pressure distributions showed that the stator diffusion process occurred smoothly and continuously, with subsonic flow throughout.

Once the steady operation of the cascade was verified, it was then necessary to match the shock conditions in the cascade to the bow shock in the actual compressor. The orientation of the shock relative to the cascade was measured using shadowgraph photography and wall-mounted Kulite pressure transducers. After a few adjustments to the shock shaper, the shock angle matched the desired 37º from axial. The actual compressor operating at design conditions had a shock strength of 1.47, but this value was unattainable in the experiment due to the available diaphragm thicknesses and run-to-run variation in the diaphragm rupture pressure. However, tests were conducted for three different diaphragm thicknesses, which resulted in three shock strengths: 1.42, 1.76, and 2.10. By using a range of shock strengths, relationships between shock strength and the resulting flow field could be determined, which proved to be more valuable than the flow behavior at the precise shock strength of 1.47.

The effects of the moving shock on the stator flow field were measured qualitatively using shadowgraphy and quantitatively using Digital Particle Image Velocimetry. The shadowgraph images demonstrated how the shock turned normal to the flow as it propagated upstream, while revealing the formation of a vortex near the trailing edge after the shock passed. DPIV was used to detail the flow field in the trailing edge region as the vortex formed and propagated downstream. Analysis of the DPIV

results showed that the vortex formed for each shock strength, and that the size of the vortex was directly related to the shock strength.

The DPIV results were used to identify probable loss mechanisms and estimate the extent of these losses. Two primary loss mechanisms were identified: the vortex that forms as the shock passes the stator trailing edge, and the upstream-propagating normal shock in the stator passage. Streamlines were plotted in the vortex region to estimate an effective blockage size due to the vortex, which propagated downstream slower than the surrounding flow. The extent of this blockage ranged from 2.9% of the passage for the weakest shock, to 14.3% of the passage for the strongest shock. In addition to blockage, the vortex was shown to cause flow angle deviation up to 75º for the greatest shock strength. Crocco's Theorem was applied to relate flow vorticity to stagnation pressure losses in the vortex region, leading to the conclusion that the vortex-induced stagnation pressure losses ranged from 46% to 113% of the steady wake losses. Finally, stagnation pressure losses due to the upstream-propagating normal shock were estimated to be approximately 0.22% of the local absolute total pressure. While it is difficult to precisely quantify the overall stator losses due to the shock-passing event, the low efficiency in close-stage-spacing transonic compressors is likely due to a combination of the two loss mechanisms presented above.

Some important distinctions must be drawn between the current work and the experiments conducted by Estevadeordal et al. (2002) at the Air Force Research Laboratory's SMI rig. The wake generators used in the AFRL experiments were unloaded, symmetric airfoils with blunt trailing edges, whereas the current work involves a loaded stator geometry. The shocks in the AFRL experiments were produced in the same manner as in an actual aircraft engine (using a transonic rotor stage), while the current work simulates the rotor bow shock using a single moving shock wave generated externally in a shock tube. The vortices which Estevadeordal et al. encountered downstream of the wake generators were shed simply due the blunt trailing edge geometry, although the vortex-shedding frequency was dictated by the rotor blade-passing frequency. In the current work, the vortex that forms downstream of the stator trailing edge is solely due to the shock-passing event, and does not occur under steady operation.

The question that remains unanswered is how the results from these experiments involving a single shock in a linear cascade transfer to the rotating environment of an actual compressor with periodic shocks. The expansion waves which follow the bow shock in the compressor were not modeled in the experiment and may have a significant impact on if, or how, the vortex forms. The vortex in the experiments is still a significant part of the trailing edge flow field at the time the next shock would be passing in the actual compressor, but how periodic shocks would influence existing vortices remains unknown and could be an interesting topic for future work.

Finding solutions to the problem of high losses in transonic compressors with close stage spacing will likely be a topic of much attention in coming years. The easiest solution, which has been the norm in the past, has simply been to maintain a fairly large axial distance between the stator row and the downstream transonic rotor. However, the aircraft engine industry, which strives to continually reduce engine size and weight while increasing thrust and efficiency, does not deem this to be an acceptable long-term solution. Serrated, porous, or even actuated stator trailing edges could offer improvements, but only continued research into the nature of the problem will lead to the development of a valid solution.

References

Anderson, J.D., Modern Compressible Flow, McGraw-Hill, 1982, pp. 202-203.

Chester, W., "The Propagation of Shock Waves along Ducts of Varying Cross Section," Advances in Applied Mechanics VI, 1960, pp. 119-152.

Doughty, R.L., "Effects of Multiple Incident Shock Waves on the Flow in a Transonic Turbine Cascade," Ph.D. Dissertation, Virginia Polytechnic Institute and State University, Blacksburg, VA, 1994.

Douglas, J.W., "Effects of Free Stream Turbulence on Compressor Cascade Performance," M.S. Thesis, Virginia Polytechnic Institute and State University, Blacksburg, VA, 2001.

Estevadeordal, J., Gogineni, S., Goss, L., Copenhaver, W., and Gorrell, S., "Study of Wake-Blade Interactions in a Transonic Compressor Using Flow Visualization and DPIV," ASME Journal of Fluids Engineering, 2002, Vol. 124, pp. 166-175.

Figliola, R.S., and Beasley, D.E., Theory and Design for Mechanical Measurements, John Wiley & Sons, 2000, pp.367-368.

Gorrell, S.E., Okiishi, T.E., and Copenhaver, W.W., "Stator-Rotor Interactions in a Transonic Compressor: Part 1-Effect of Blade-row Spacing on Performance," GT-2002-30494, ASME Turbo Expo, Amsterdam, The Netherlands, June 3-6 2002.

Gorrell, S.E., Okiishi, T.E., and Copenhaver, W.W., "Stator-Rotor Interactions in a Transonic Compressor: Part 2-Description of a Loss Producing Mechanism," GT-2002-30495, ASME Turbo Expo, Amsterdam, The Netherlands, June 3-6 2002.

Kerrebrock, J.L., "Flow in Transonic Compressors," AIAA Journal, 1981, Vol. 19, pp. 4-19.

Liepmann, H.W., and Roshko, A., Elements of Gasdynamics, John Wiley & Sons, 1967, pp. 190-196.

Nettleton, M.A., "Shock Attenuation in a Gradual Area Expansion," Journal of Fluid Mechanics, 1973, Vol. 60, pp. 209-223.

Oosthuizen, P.H., and Carscallen, W.E., Compressible Fluid Flow, McGraw-Hill, 1997, pp. 62-64, 88-113.

Prasad, A., "Evolution of Upstream Propagating Shock Waves From a Transonic Compressor Rotor," ASME Journal of Turbomachinery, 2003, Vol. 125, pp. 133-140.

Sabersky, R.H, Acosta, A.J., Hauptmann, E.G., and Gates, E.M., Fluid Flow, 4th Ed., Prentice Hall, 1999, pp. 30-34.

Schetz, J.A., Boundary Layer Analysis, Prentice-Hall, 1993, pp. 9-22.

Settles, G.S., Schlieren and Shadowgraph Techniques, Springer-Verlag, 2001.

Sloan, S.A., and Nettleton, M.A.,"A Model for the Axial Decay of a Shock Wave in a Large Abrupt Area Change," Journal of Fluid Mechanics, 1975, Vol. 71, pp. 769-785.

Appendix A: MATLAB Code used for Angle Probe Data Reduction

```
% L Angle Probe data reduction - modified
% Written by Bo Song
% Input: Po,Pu,Pd from load file
% Output: Pt, Ps, Ma, Angle(Ang)
% This code is good for the range: Mach(0.1-1) Angle:(-
12deg-12deg)
I=3933;
Patm=0;
load a.txt;
Po=a(:,1);
Pu=a(:,2);
Pd=a(:,3);
Maknot=[0.1,0.2,0.3,0.4,0.5,0.6,0.7,0.8,0.9,1.0];
Pm=(Pu+Pd)/2;
Q=Po-Pm;
f1=(Pu-Pd)./Q;
Ang=50.641*f1.^5+4.6878*f1.^4-38.275*f1.^3-
2.8969*f1.^2+25.572*f1-0.004;
f2=7e-7*Ang.^4-2e-6*Ang.^3+1e-5*Ang.^2+1e-4*Ang+4e-4;
Pt=f2.*Q+Po;
f3knot(:,1)=-3E-07*Ang.^2 + 2E-05*Ang + 1.0031;
f3knot(:,2)=-5E-06*Ang.^2 + 5E-05*Ang + 1.0183;
f3knot(:,3)=-9E-06*Ang.^2 + 0.0001*Ang + 1.0441;
f3knot(:,4)=-8E-06*Ang.^2 + 0.0002*Ang + 1.0786;
f3knot(:,5)=3E-06*Ang.^2 + 0.0003*Ang + 1.1198;
f3knot(:,6)=3E-05*Ang.^2 + 0.0004*Ang + 1.166;
f3knot(:,7)=7E-05*Ang.^2 + 0.0006*Ang + 1.2151;
f3knot(:,8)=0.0001*Ang.^2 + 0.0007*Ang + 1.2653;
f3knot(:,9)=0.0002*Ang.^2 + 0.0009*Ang + 1.3147;
f3knot(:,10)=0.0004*Ang.^2 + 0.0012*Ang + 1.3614;

for i=1:I,
   i
   f3(i)=(Pt(i)+Patm)/(Pm(i)+Patm);
   Ma(i)=spline(f3knot(i,:),Maknot,f3(i));
   Ps(i)=(Pt(i)+Patm)/((1+0.2*Ma(i)^2)^3.5)-Patm;
end

Ma=Ma';
Ps=Ps';
output(:,1)=Pt;
output(:,2)=Ps;
output(:,3)=Ma;
output(:,4)=Ang;
save output output -ascii
```

Appendix B: Blade Surface Static Pressure Distributions at Off-Design Incidence

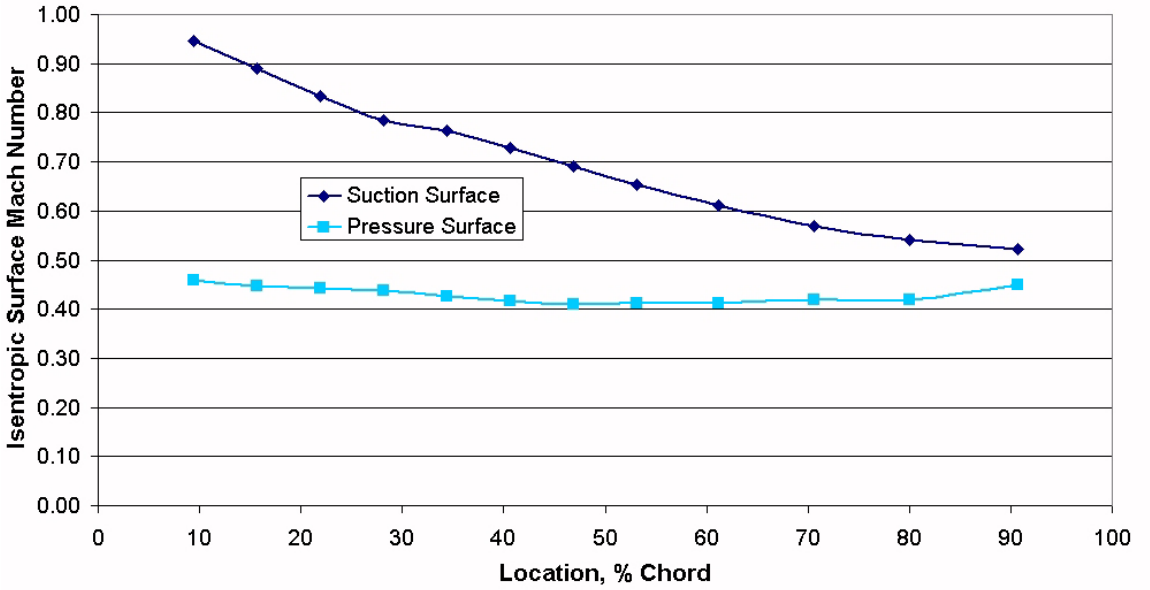

Figure B.1: Isentropic Mach number distribution along blade surface at +5° incidence.

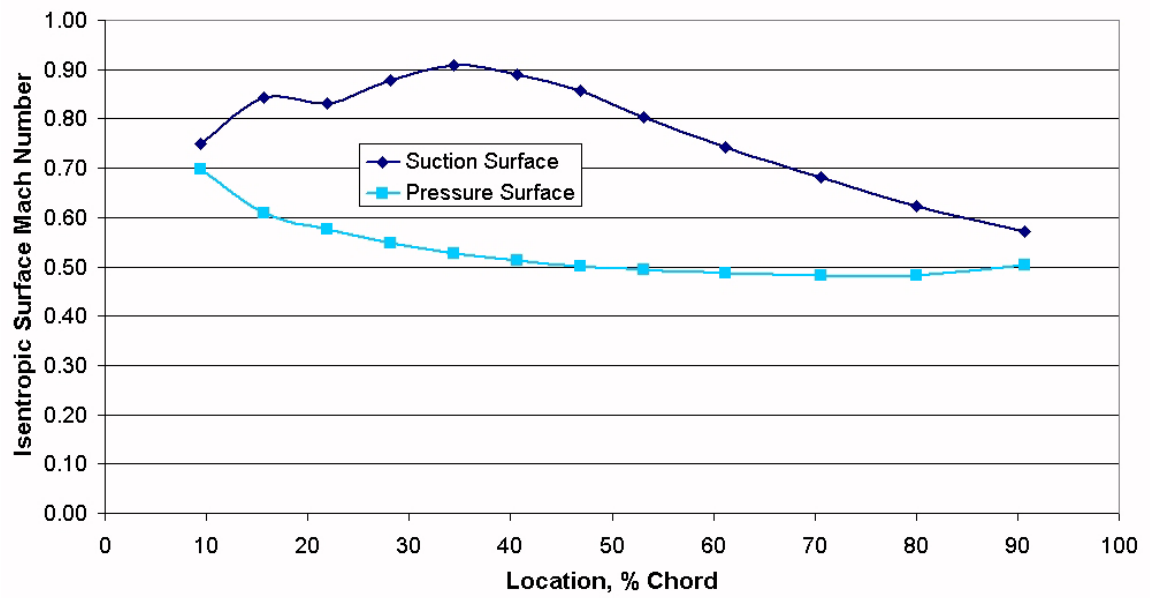

Figure B.2: Isentropic Mach number distribution along blade surface at -5° incidence.

Appendix C: Uncertainty Analysis

The following is an uncertainty analysis of the parameters measured for the cascade experiments. Bias errors exist for all measurements in this experiment, but were minimized as much as possible through careful measurement range selection and frequent calibration. Quantization errors due to the A/D conversion process were always negligible when compared to the transducer error, and are therefore disregarded for this section. Table C.1 summarizes the bias errors of the various measurements for this experiment.

Table C.1: Bias errors due to instrument uncertainty.

Measurement(s)	Instrument	Instrument Uncertainty
Blade Surface Static Pressures	Pressure Systems International 8400 0-15 psid	+/- .001 psi
P_{01}*, P_{02}, P_{up}, P_{down}	MKS Pressure Transducer 0-20 psid	+/- .01 psi
P_1*, ΔP_0 (P_{01} - P_{02})	MKS Pressure Transducer 0-3 psid	+/- .005 psi
Ps_1, Ps_2	Kulite XCL-072 Pressure Transducer 0-50 psig	+/- .05 psi
Incidence Angle	Digital Protractor	+/- .05°
Transducer Calibration	Fluke 0-30 psi Calibrator	+/- .015 psi

*P_1 and P_{01} were measured using the Pressure Systems International for all runs except the downstream angle probe measurements, which used the MKS transducers instead.

The parameters M and ω are calculated using multiple pressure measurements, so the errors of these measurements are compounded and propagated in the resulting parameter by the following equations:

Equation C.1
$$\delta\omega = \sqrt{\left[\left(\frac{\partial \varpi}{\partial \Delta P_0}\right)\delta P_0\right]^2 + \left[\left(\frac{\partial \varpi}{\partial P_{01}}\right)\delta P_{01}\right]^2 + \left[\left(\frac{\partial \varpi}{\partial P_1}\right)\delta P_1\right]^2}$$

Equation C.2
$$\delta M = \sqrt{\left[\left(\frac{\partial M}{\partial P_0}\right)\delta P_0\right]^2 + \left[\left(\frac{\partial M}{\partial P_1}\right)\delta P_1\right]^2}$$

Evaluating Equations C.1 and C.2 yields the maximum propagated uncertainties in Mach number and Total Pressure Loss Coefficient given in Table C.2.

Table C.2: Maximum propagated uncertainty.

Calculated Parameter	Maximum Propagated Uncertainty
Inlet Mach Number, Angle Probe Traverse Runs	+/- .0008
Inlet Mach Number, All Other Runs	+/- .001
Isentropic Surface Mach Number	+/- .001
Total Pressure Loss Coefficient, ω	+/- .001

Vita

Matthew D. Langford

Matthew D. Langford was born in Lynchburg, Virginia on May 18th, 1980, to John and Joanne Langford. He attended E.C. Glass High School in Lynchburg, Virginia, and graduated in 1998. He graduated from Virginia Polytechnic Institute and State University in 2002 with *Summa Cum Laude* distinction, with a Bachelor of Science Degree in Mechanical Engineering. Upon completing his M.S. research and coursework, he will begin work as a research engineer at Techsburg, Inc. in Blacksburg, Virginia.